Multi-scale investigation of winter balance on alpine glaciers

by

Alexandra Pulwicki

B.Sc., University of Calgary, 2014

Dissertation Submitted in Partial Fulfillment of the
Requirements for the Degree of
Master of Science

in the
Earth Science
Faculty of Science

© Alexandra Pulwicki 2017

SIMON FRASER UNIVERSITY
Summer 2017

Copyright in this work rests with the author. Please ensure that any reproduction or re-use is done in accordance with the relevant national copyright legislation.

Approval

Name: **Alexandra Pulwicki**

Degree: **Master of Science (Earth Science)**

Title: **Multi-scale investigation of winter balance on alpine glaciers**

Examining Committee: **Chair:** ??
??

Gwenn Flowers
Senior Supervisor
~~Associate~~ Professor

Valentina Radic
Committee Member
Associate Professor

Kirsten Zickfeld
Committee Member
Associate Professor

??
External Examiner
Professor
Department of Quantum Fields
Mars University

Date Defended: **??**

Abstract

Accurately estimating winter surface mass balance on glaciers is central to assessing glacier health and predicting glacier runoff. However, measuring and modelling snow distribution is inherently difficult. Here I explore rigorous statistical methods of estimating winter balance and its uncertainty from multiscale measurements of snow depth and density. In May 2016 we collected over 9000 manual measurements of snow depth across three glaciers in the St. Elias Mountains, Yukon, Canada. Linear regression, combined with cross correlation and Bayesian model averaging, as well as simple kriging and regression kriging are used to interpolate point-scale values. Elevation and a wind-redistribution parameter exhibit the highest correlations with winter balance, but the relationship varies considerably between glaciers. A Monte Carlo analysis reveals that the interpolation itself introduces more uncertainty than the assignment of snow density or the representation of grid-scale variability. Despite challenges associated with estimating winter balance, ~~my~~ results are consistent with a regional-scale winter-balance gradient.

Keywords: glacier; snow; winter balance; spatial statistics; regression

Acknowledgements

I thank the Kluane First Nation (KFN), Parks Canada and the Yukon Territorial Government for granting me permission to work in KFN Traditional Territory and Kluane National Park and Reserve. I am grateful for financial support provided by the Natural Sciences and Engineering Research Council of Canada, Simon Fraser University and the Northern Scientific Training Program. I kindly acknowledge Kluane Lake Research Station, Sian Williams, Lance Goodwin and Trans North pilot Dion Parker for facilitating field logistics. I am grateful to Alison Criscitiello and Coline Ariagno for all aspects of field assistance and Sarah Furney for assistance with data entry. Thank you to Etienne Berthier for providing me with the SPIRIT SPOT-5 DEM and for assistance in DEM correction. I am grateful to Derek Bingham and Michael Grosskopf for assistance with the statistics, including simple kriging. A big thank you to Luke Wonneck for being my unfailing source of new perspectives and motivating ideas. Thank you to all the members of the SFU Glaciology group for their steady supply of positive energy, outdoor adventures and lunch-time discussions. Finally, I would like to thank Gwenn Flowers for her tireless support, kind words of encouragement and firm commitment to producing quality work. Her strength and dedication are an inspiration.

Table of Contents

Approval ii

Abstract iii

Acknowledgements iv

Table of Contents v

List of Tables ix

List of Figures xii

1 Introduction 1

- 1.1 Accumulation variability . . . 2
  - 1.1.1 Topographic scales . . . 2
  - 1.1.2 Snow drift and preferential deposition . . . 3
- 1.2 Snow distribution models . . . 4
  - 1.2.1 Dynamic models . . . 4
  - 1.2.2 Statistical models . . . 5
- 1.3 Measuring accumulation . . . 8
  - 1.3.1 Snow probing . . . 9
  - 1.3.2 GPR . . . 13
  - 1.3.3 DEM subtraction . . . 15
  - 1.3.4 Comparison of methods . . . 17
  - 1.3.5 Temporally resolved methods . . . 18
- 1.4 Snow distribution on glaciers . . . 19
- 1.5 Glaciers in the St. Elias Mountains . . . 21
- 1.6 Research scope . . . 27
  - 1.6.1 Overview of research . . . 27
  - 1.6.2 Thesis structure . . . 28
- 1.7 Summary . . . 28

2 Field methods and data processing 30

2.1 Experimental design 31
  2.1.1 Sampling Scheme and Naming System 31
2.2 Field methods 36
  2.2.1 Linear and Curvilinear Transects 36
  2.2.2 Zigzag 43
  2.2.3 Federal Snow Sampler 43
  2.2.4 Firn Corer 46
  2.2.5 Snow pit 47
2.3 Data processing 50
  2.3.1 Snow depth measured with graduated avalanche probe 50
  2.3.2 Snow density 51
  2.3.3 Point-scale winter balance 52
2.4 Topographic parameters 54
  2.4.1 Obtaining digital elevation models (DEMs) for study glaciers 54
  2.4.2 Calculating topographic parameters 57
  2.4.3 DEM smoothing 64
  2.4.4 Parameter correlations 65
  2.4.5 Maps of topographic parameters and distribution of parameters sampled 66
2.5 Summary 76

3 Sampling **78**
3.1 Density 78
  3.1.1 Basic statistics 78
  3.1.2 Federal Sampler measurements and snow depth 78
  3.1.3 Density uncertainties 79
  3.1.4 Comparing density from snow pit and Federal Sampler measurements 82
  3.1.5 Density and elevation 82
3.2 Linear and curvilinear transect snow depth data 86
3.3 Zigzag snow depth data 87
3.4 Point-scale winter balance 90
3.5 Variability at multiple scales 96
  3.5.1 Point-scale variability 97
  3.5.2 Gridcell-scale variability 98
3.6 Summary 102

4 Interpolation **104**
4.1 Linear topographic regressions 104
  4.1.1 Background 104
  4.1.2 Importance of variables in regression models 105
  4.1.3 Multiple Linear Regression (MLR) 106

4.1.4 Bayesian Model Averaging (BMA) 119
4.1.5 MLR and BMA comparison 131
4.1.6 Number of cross validation runs 133
4.2 Kriging 133
4.2.1 Background 133
4.2.2 Methods 135
4.2.3 Results 135
4.3 Regression kriging 138
4.3.1 Background 138
4.3.2 Methods 139
4.3.3 Results 139
4.4 Comparison of interpolation methods 142
4.5 Summary 145

5 Winter balance **147**
5.1 Methods 147
5.2 Results 149
5.2.1 Winter balance uncertainty 149
5.2.2 Spatial patterns of winter balance uncertainty 151
5.3 Discussion 152
5.4 Summary 152

6 Regional Controls **154**
6.1 Transferability of linear regression coefficients 154
6.2 Regional winter-balance gradient 158
6.3 Summary 159

7 Conclusion **160**
7.1 Significance and strengths 160
7.2 Limitations and future work 161
7.3 Summary 164

Bibliography **166**

Appendix A GPS Waypoint Creation and Upload to GPS Device **177**

Appendix B Field Maps **179**

Appendix C Data Processing Scripts **192**
C.1 Snow depth measured with graduated avalanche probe 192
C.1.1 Linear and curvilinear transect surveys 192

C.1.2 Zigzag surveys 193
C.2 Snow density 194
C.3 Point-scale winter balance 195

Appendix D Topographic parameters from QGIS to Matlab 197

Appendix E MLR software 198

Appendix F BMA software 200

Appendix G Kriging software 202

Appendix H Variability of data at various scales 203
H.1 Point Scale 203
H.1.1 Data normality 203
H.1.2 Observer differences 203
H.1.3 Standard deviation of snow depth along linear and curvilinear transects 204
H.1.4 Standard deviation of WB in DEM cell 205

Appendix I Winter surface mass balance distribution 209
I.1 Linear regression winter balance distribution 210
I.2 Simple kriging winter balance distribution 214

List of Tables

Table 1.1 Relevant spatial scales for snow variability on glaciers. Information from Clark and others (2011). 3

Table 1.2 Physical characteristics of the study glaciers and May 2016 winter-balance survey details, including number of snow-depth measurement locations along transects (n_{T}), total length of transects (d_{T}), number of combined snow pit and Federal Sampler density measurement locations (n_ρ) and number of zigzag surveys (n_{zz}). 26

Table 2.1 Summary information for snow depth transects. Transect shapes completed include Lower Hourglass (LH), Lower Circle (LC), Lower Midline (LM), Upper Hourglass (UH), Upper Circle (UC), Upper Midline (UM), Upper Transect (UT) and Bonus Transect (BT). The first observer was navigating to waypoints and the remaining three were taking depth measurements. 41

Table 2.2 Summary information for zigzag measurements 42

Table 2.3 Summary information for Federal Sampler measurements 45

Table 2.4 Statistics of integrated densities measured using Federal Sampler or vertical density profiles (of snow wedge measurmenets) in snow pits. Mean, standard deviation (std) and number (n) of snow density (kg m^{-3}) measurements on study glaciers is shown. 52

Table 2.5 Eight methods used to estimate snow density at unmeasured locations. Total number of resulting density values given in parentheses, with n_T the total number of snow-depth measurement locations along transects (Table 1.2). 54

Table 2.6 Description of topographic parameters used in the linear regression. . 63

Table 2.7 Values of azimuth (A) and maximum search distance ($d$max), that correspond to the Sx that had the highest absolute correlation to observed WB. 64

Table 2.8 Pearson correlation coefficients between topographic parameters at sampled locations. Topographic parameters are distance from centreline (d_C), elevation (z), aspect (α), slope (m), northness (N), curvature (κ) and wind redistribution (Sx). 66

Table 2.9 Descriptive statics of topographic parameter full and sampled distribution. Mean and standard deviation are in units of meters for distance from centreline (d_C) and elevation (z), in units of m^{-1} for profile (κ_P) and tangential (κ_T) curvature and are unitless for cosine of aspect (α), "northness" (N), slope (m) and wind redistribution (Sx). Skewness is a measure of the data asymmetry about the mean, with positive values indicating data that are more spread to the right of the mean and zero indicating a perfectly symmetric distribution. Kurtosis is a measure of how prone a distribution is to outliers. A normal distribution has a kurtosis value of 3 and larger values indicate distributions that are more prone to outliers. 69

Table 3.1 Summary of integrated snow density values calculated from snow pit measurements. The reference density values are calculated with an ice layer density of 917 kg m^{-3} and a 'hard' snow density of 600 kg m^{-3}. To determine the error in estimating integrated snow density, ice density, ice thickness and the 'hard' layer density are varied between 700 and 917 kg m^{-3}, ± 1 cm and 500 and 600 kg m^{-3}, respectively. . 81

Table 3.2 Range of densities estimated from Federal Sampler measurements. The number (n) of reliable measurements, as well as the minimum, maximum and mean density are shown. The density range, given as a percent of the mean density, is also shown. Location refers to the snow pit name as shown in Figure 2.9. 83

Table 3.3 Summary of linear regressions between integrated density and elevation (m a.s.l.). 84

Table 3.4 2σ values of winter balance variability (m w.e.) distributions at the point and gridcell scale. 97

Table 4.1 Mean MLR and BMA coefficients for regression of winter balance (WB) data on standardized topographic parameters. Topographic parameters are distance from centreline (d_C), elevation (z), aspect (α), slope (m), northness (N), curvature (κ) and wind redistribution (Sx). Since parameters are standardized, the magnitude of the coefficients is representative of their importance in predicting WB. The root-mean-squared error (RMSE) between modelled WB using those coefficients and observed WB is also given. Semi-partial correlation is a metric that describes the increase in R^2 from the addition of a parameter to a regression that contains all other regressors. Raw correlation is the square of the Pearson correlation between a parameter and WB. 108

Table 4.2 MLR coefficients for regression of winter balance (WB) data on standardized topographic parameters. Topographic parameters are distance from centreline (d_C), elevation (z), aspect (α), slope (m), northness (N), curvature (κ) and wind redistribution (Sx). Since parameters are standardized, the magnitude of the coefficients is representative of their importance in predicting WB. The root-mean-squared error (RMSE) between modelled WB using those coefficients and observed WB is also given. See Table 2.5 for description of density assignment methods. 109

Table 4.3 BMA coefficients for regression of WB data and standardized topographic parameters. Topographic parameters are distance from centreline (d_C), elevation (z), aspect (α), slope (m), northness (N), curvature (κ) and wind redistribution (Sx). Since parameters are standardized, the magnitude of the coefficients is representative of their importance in predicting WB. The root-mean-squared error (RMSE) between modelled WB using those coefficients and observed WB is also given. See Table 2.5 for description of density assignment methods. 123

Table 4.4 ANOVA p-values between estimated WB found using MLR and BMA regression coefficients for various density assignment methods. 132

Table 4.5 Nugget ($\times 10^{-3}$ m w.e.) and range length (m) values for WB data with various snow density assignment methods estimated using maximum likelihood in `DiceKriging` package. S = Snow pit density values, F = Federal Sampler density values. See Table 2.5 for details on density assignment methods. 137

Table 5.1 Standard deviation ($\times 10^{-2}$ m w.e.) of glacier-wide winter balance distributions arising from uncertainties in grid-scale WB (σ_{GS}), density assignment (σ_ρ), interpolation (σ_{INT}) and all three sources combined (σ_{ALL}) for linear regression (left columns) and simple kriging (right columns) 149

Table 6.1 Elevation regression coefficients and intercepts used in linear regression transferability. The total root mean squared error (RMSE) for all glaciers arising from each set of regression coefficients is also given. . 155

List of Figures

Figure 1.1 Digging a snow pit in the accumulation area of Haig Glacier, Rocky Mountains . . . 9

Figure 1.2 Examples of snow sampling schemes. Figures (a), (b), (c) and (e) from Shea and Jamieson (2010). Figure (d) from Schweizer and others (2008a). Figure (f) from Parr, C., (2016 personal communication). 12

Figure 1.4 Radargram from the accumulation area of Findelengletscher, Valais, Switzerland. (a) The reflection at the air-snow interface. (b) The reflection at the snow-ice interface. Figure taken from Sold and others (2013). . . . 15

Figure 1.3 Schematic diagram of a helicopter-borne radar snow survey. The travel time for the signal to interact with the snow surface is shown as a solid line and the signal travel time of the interaction with the ice is shown as a dashed line. Together, these values can be used to determine snow depth. The inset (a) is an example waveform that would be recorded from these two events. Figure taken from Gusmeroli and others (2014). . . . 15

Figure 1.5 Schematic of airborne LiDAR system geometry. Scan angle (θ), height (h) and swath width (SW) are shown. Figure from Deems and Painter (2006). . . . 16

Figure 1.6 Map of the St. Elias Mountains and surrounding area. Figure taken from Danby and others (2003). . . . 22

Figure 1.7 Visualization of four spatial scales investigated in project. The lower panels show examples of the amount of data analysed at each scale. 27

Figure 1.8 Visual representation of research project. General scope is described on the left (ovals) and specific investigations are shown on the right (squares). . . . 29

Figure 2.1 Study glaciers in the Donjek Range, Yukon (see inset). The topographic divide is shown as a dashed line. . . . 33

Figure 2.2 Planned sampling design. Target waypoints for snow depth transects, snow pits and Federal Sampler measurements are shown for the three study glaciers. . . . 34

Figure 2.3 Randomly assigned locations for zigzag measurements in the ablation area (divided into seven zones). 35
Figure 2.4 Example of zigzag. Vertices are labelled and measurements are taken at random intervals along the dashed lines between vertices. The randomly chosen location of the Federal Sampler measurement is shown as a diamond. 37
Figure 2.5 Implementation of transect probing. The first person navigated to the intended waypoint using the GPS device. The second, third and fourth (not seen) observers are probing using 3.2 m long avalanche probes. There is approximately 10 m between observers. Photo credit: G. Flowers 39
Figure 2.6 Schematic of the snow depth measurement configuration. Blue circles indicate depth measurement and orange squares indicate waypoint (WP) location. 40
Figure 2.7 Snow depth values measured along a zigzag pattern (G04_Z3A) . . 44
Figure 2.8 Using the Federal Sampler to measure snow water equivalent 44
Figure 2.9 Locations and labels for all snow pits dug on Glaciers 4, 2 and 13 (left to right). 48
Figure 2.10 Taking snow denisty measurements in a snow pit. An expandable ruler is used to measure snow depth and determine sampling locations. A 250cc wedge cutter is used to extract a known volume of snow and a spring scale is used to weigh the snow. The dial-stem thermometer is used for measureing snow temperature. Note that the sampling wall is shaded, has an undistrubed snow surface above it and has a smoothed face. Photo credit: A. Criscitiello 49
Figure 2.11 Example of estimating snow depth measurement locations in one area (indicted by black box) on Glacier 13. Numbered waypoint (WP) locations are shown in blue and estimated measurement locations are shown in orange at a distance of 10, 20 and 30 m from the WP. Measurement locations are taken to be along a straight line between subsequent WPs. For the first WP of a transect, the measurement locations are assumed to be along the same line as that between the first and second WPs of a transect. For example, the measurement locations behind WP 660 fall along the same line as those between WP 660 and WP 661. The same is true for WP 745. 50

Figure 2.12 Example of zigzag survey measurement locations calculated using difference reference vertices for each section of the zigzag. Black squares show measurement locations calculated using the original GPS coordinates of vertices (Option 1). Blue circles show measurement locations calculated using the last measurement location from the previous section as the reference vertex (Option 2). For the first and fifth vertices (located at (0, 40 m) and (0, 4 m)) the original GPS coordinates were used for both options. 51

Figure 2.13 Relationship between various ways to interpolate between density measurements for the calculation of point-scale winter balance. The bottom row shows the code for each density interpolation option as described in Section 2.3.3. 52

Figure 2.14 SPOT-5 DEMs available for the Donjek Range. Study glaciers are shown as red outlines. The DEM made from imagery collected on September 3, 2007 (GES 08-029) is shown in (a) and the DEM made from imagery collected on September 13, 2007 (GES 07-044) is shown in (b). Imagery that contains cloud cover result in a distorted DEM, as seen in the boxed area of (a). 55

Figure 2.15 Landsat 7 ETM images of study glaciers on September 13, 2007. Snow cover is shown as light blue and ice is shown as dark blue. . . 55

Figure 2.16 Vertical difference between DEMs in overlapping area. Difference was found by subtracting GES 08-029 from GES 07-044. Positive values indicate that GES 07-044 values are higher than GES 08-029 values. 56

Figure 2.17 Histogram of the vertical difference between GES 08-029 and GES 07-044 before (dark blue) and after (light blue) correction. 56

Figure 2.18 Outlines of the cropped GES 07-044 DEM (pink, left) and cropped GES 08-029 DEM (blue, right) used for merging. There is a slight overlap between the two DEMs that cannot be seen at this scale. . 57

Figure 2.19 Merged DEM of the Donjek range from two corrected SPOT-5 DEMs, plotted with 10 m contour lines. Study glaciers are shown in red. Discrepancies between the DEMs along the merge line can be seen as anomalous linear features in the contour map (yellow boxes). Distorted contours in the eastern regions (white box) are a result of errors in the DEM. 58

Figure 2.20 Labelling of DEM gridcells surrounding the cell of interest. The eight surrounding cells are used for estimating topographic parameters in QGIS. The cell of interest, which is located at row i and column j of the DEM, is shown as a shaded cell and is labelled z_5. 60

Figure 2.21 Example of Sx calculations for three cells of interest along a 270° search vector. As depicted, with $d$max set equal to 300 m, the shelter-defining pixel for cells 1 and 2 is cell A, producing positive Sx values. The shelter-defining cell for cell 3 is cell B, producing a negative Sx. Had $d$max been equal to 100 m, the search for the shelter-defining pixel for cell 1 would not extend across the valley, thus producing a negative Sx for cell 1, while Sx for cell 2 would remain the same and that for cell 3 would be slightly lower. Image and description from (Winstral and others, 2002). 64

Figure 2.22 (a) Curvature found using the orginal DEM. (B) The smoothed (7×7 window moving average) DEM. 65

Figure 2.23 Distributions of elevation (z) used in the topographic regressions for the study glaciers. This DEM is derived from a SPOT5 satellite image and has a grid size of 40×40 m. Subsequent topographic parameters were derived from this DEM. Arrows indicate glacier flow direction and black dots show snow depth sampling locations. 70

Figure 2.24 Histograms of elevation (z) sampled (black) as compared to total range of elevation (white) of study glaciers. 70

Figure 2.25 Distributions of distance from centreline (d_C) used in the topographic regressions for the study glaciers. Centreline was drawn by hand in QGIS. Arrows indicate glacier flow direction and black dots show snow depth sampling locations. 71

Figure 2.26 Histograms of distance from centreline (d_c) sampled (black) as compared to total range (white) of distance from centreline of study glaciers. 71

Figure 2.27 Distributions of the sine of aspect (α), which indicates north-south component of a slope (+1 defined as north), used in the topographic regressions for the study glaciers. Values are derived from a smoothed DEM. Arrows indicate glacier flow direction and black dots show snow depth sampling locations. 72

Figure 2.28 Histograms of aspect (α) sampled (black) as compared to total range (white) of aspect of study glaciers. 72

Figure 2.29 Distributions of slope (m) used in the topographic regressions for the study glaciers. Values were derived from a smoothed DEM (grid size of 40×40 m) in QGIS. Arrows indicate glacier flow direction and black dots show snow depth sampling locations. 73

Figure 2.30 Histograms of slope (m) sampled (black) as compared to total range (white) of slope of study glaciers. 73

Figure 2.31 Distributions of “northness” (N) used in the topographic regressions for the study glaciers. “Northness” is defined as the product of the cosine of aspect and sine of slope. A value of -1 represents a steep, south facing slope, a value of +1 represents a steep, north facing slope and flat surfaces yield 0. Values were derived from a smoothed DEM (grid size of 40×40 m) in QGIS. Arrows indicate glacier flow direction and black dots show snow depth sampling locations. . . . 74

Figure 2.32 Histograms of “northness” (N) sampled (black) as compared to total range (white) of “northness” of study glaciers. 74

Figure 2.33 Distributions of curvature (κ) used in the topographic regressions for the study glaciers. Values were derived from a smoothed DEM (grid size of 40×40 m) in QGIS. Colour axis has been scaled to better resolve values close to zero. Arrows indicate glacier flow direction and black dots show snow depth sampling locations. 75

Figure 2.34 Histograms of curvature (κ) sampled (black) as compared to total range (white) of profile curvature of study glaciers. 75

Figure 2.35 Distributions of Sx, which is a wind redistribution parameter, used in the topographic regressions for the study glaciers. See Section 2.4.2 and the original paper by Winstral and others (2002) for more details on calculation. See Table 2.7 for values of best correlated azimuth and maximum search distance for each glacier. Arrows indicate glacier flow direction and black dots show snow depth sampling locations. 76

Figure 2.36 Histograms of Sx sampled (black) as compared to total range (white) of Sx of study glaciers. 76

Figure 3.1 Relationship between measured density and snow depth for all Federal Sampler and snow pit locations. A linear regression of depth and density for Federal Sampler measurements is shown as a solid line and for snow pits is shown as a dashed line. 80

Figure 3.2 Comparison of depth-averaged densities estimated using Federal Sampler (FS) measurements and a wedge cutter in a snow pit (SP) for Glacier 4 (G4), Glacier 2 (G2) and Glacier 13 (G13). Labels indicate snow pit locations in the accumulation area (ASP), upper ablation area (USP) and lower ablation area (LSP). Error bars for SP-derived densities are calculated by varying the thickness and density of layers that are too hard to sample (Table 3.1) and error bars for FS-derived densities are the standard deviation of measurements taken at one location (Table 3.2). One-to-one line is dashed. 84

Figure 3.3 Relationship between measured snow depth and elevation at all sampling locations for Glaciers 4 (G04), 2 (G02) and 13 (G13). 85
Figure 3.4 Relationship between snow pit-derived density and elevation for Glaciers 4 (G04), 2 (G02) and 13 (G13). 85
Figure 3.5 Relationship between Federal Sampler-derived density and elevation for Glaciers 4 (G04), 2 (G02) and 13 (G13). 86
Figure 3.6 Boxplots of snow depth measured on study glaciers. (a) All snow depth values. (b) Snow depth values only from transects (zigzag, snow pit and Federal Sampler measurements excluded). Red line indicates median, blue box shows first quantiles, bars indicate minimum and maximum values (excluding outliers) and red crosses show outliers, which are defined as being outside of the range of 1.5 times the quartiles (approximately $\pm 2.7\sigma$). 86
Figure 3.7 Boxplots of snow depth data measured at each zigzag location. See Figure 3.8 for locations of each zigzag. 87
Figure 3.8 Map of zigzag locations on Glaciers 4, 2 and 13 (left to right). . . . 88
Figure 3.9 Snow depths measured in zigzags on Glacier 4. Mean depth ($\bar{z}$) is also reported. Zigzag elevations (left to right) are 2162, 2229 and 2360 m a.s.l. See Figure 3.8 for locations of each zigzag. 89
Figure 3.10 Snow depths measured in zigzags on Glacier 2. Mean depth ($\bar{z}$) is also reported. Zigzag elevations (left to right) are 2172, 2332 and 2403 m a.s.l. See Figure 3.8 for locations of each zigzag. 89
Figure 3.11 Snow depths measured in zigzags on Glacier 13. Mean depth ($\bar{z}$) is also reported. Zigzag elevations (a-d) are 2156, 2206, 2271 and 2297 m a.s.l. See Figure 3.8 for locations of each zigzag. 90
Figure 3.12 Boxplots of estimated point-scale winter balance (WB) at sampling locations for (a) Glacier 4, (b) Glacier 2 and (c) Glacier 13. See Table 2.5 for explanation of density assignment methods and codes. Point-scale WB estimates using various density assignment methods were tested for differences using ANOVA ($p<0.05$). Point-scale WB estimates that were not significantly different are labelled with the same letter (e.g. all estimates with A on Glacier 4 are significantly different than all estimates with B on Glacier 4). 92
Figure 3.13 Estimated point-scale winter balance at measurement locations. Density was taken to be the mean value of all snow pit-derived densities from all glaciers (S1). Arrows show ice-flow direction and dashed lines show approximate ELA. Note that the individual measurement locations overlap on the figure. 93

Figure 3.14 Estimated point-scale winter balance at measurement locations. Density was taken to be the mean value of all Federal Sampler-derived densities from all glaciers (F1). Arrows show ice-flow direction and dashed lines show approximate ELA. Note that the individual measurement locations overlap on the figure. 93

Figure 3.15 Estimated point-scale winter balance at measurement locations. Density for each glacier was taken to be the mean value of snow pit-derived densities from that glacier (S2). Arrows show ice-flow direction and dashed lines show approximate ELA. Note that the individual measurement locations overlap on the figure. 94

Figure 3.16 Estimated point-scale winter balance at measurement locations. Density for each glacier was taken to be the mean value of Federal Sampler-derived densities from that glacier (F2). Arrows show ice-flow direction and dashed lines show approximate ELA. Note that the individual measurement locations overlap on the figure. 94

Figure 3.17 Estimated point-scale winter balance at measurement locations. Density was determined by using a linear fit between snow pit-derived density and elevation for each glacier (S3). Arrows show ice-flow direction and dashed lines show approximate ELA. Note that the individual measurement locations overlap on the figure. 95

Figure 3.18 Estimated point-scale winter balance at measurement locations.Density was determined by using a linear fit between Federal Sampler-derived density and elevation for each glacier (F3). Arrows show ice-flow direction and dashed lines show approximate ELA. Note that the individual measurement locations overlap on the figure. 95

Figure 3.19 Estimated point-scale winter balance at measurement locations. Density was calculated using inverse distance weighting using all snow pit-derived densities (S4). Arrows show ice-flow direction and dashed lines show approximate ELA. Note that the individual measurement locations overlap on the figure. 96

Figure 3.20 Estimated point-scale winter balance at measurement locations. Density was calculated using inverse distance weighting using all snow pit-derived densities (F4). Arrows show ice-flow direction and dashed lines show approximate ELA. Note that the individual measurement locations overlap on the figure. 96

Figure 3.21 Point-scale WB variability at measurement locations. Three to four snow depth measurement were taken at each location and converted to point-scale WB values using S1 density assignment method. . . . 97

Figure 3.22 Coefficient of variation of observations at measurement locations. Three to four snow depth measurement were taken at each location and converted to point-scale WB values using S1 density assignment method. 98
Figure 3.23 Distributions of estimated winter-balance values for each zigzag survey in lower (L), middle (M) and upper (U) ablation areas (insets). Local mean has been subtracted. (a) Glacier 4. (b) Glacier 2. (c) Glacier 13. 99
Figure 3.24 Gridcell-scale winter balance variability at the gridcell scale based on zigzag measurements. 100
Figure 3.25 Gridcell-scale winter balance variability. Transect survey data is used and variability is based on multiple measurement locations in a DEM gridcell. 100
Figure 3.26 Coefficient of variation of observations at measured gridcells. Multiple measurements locations within each gridcell are used to assess variability. 101
Figure 3.27 Number of measurement locations within DEM gridcells. 101
Figure 3.28 Winter balance variability at the gridcell scale based on eight different density assignment methods in a DEM gridcell. 102
Figure 3.29 Coefficient of variation at the gridcell scale based on eight different density assignment methods. 102

Figure 4.1 Modelled versus observed winter balance (WB). (Top row) Comparison of estimated (MLR) and observed (WB) for three study glaciers. The WB values were calculated using inverse-distance weighted snow pit densities (S4). (Bottom row) Plots of all linear fits between estimated and observed WB using eight density assignment methods. Mean R^2 value is shown for each sub-plot and a reference 1:1 line is also provided. Black line highlights the S4 option from the top row. See Figure 4.11 for a plot of all estimated WB values. 112
Figure 4.2 Summary of estimated gridcell-scale winter balance values found using MLR coefficients. Red line indicates median, blue box shows first quantiles, bars indicate minimum and maximum values (excluding outliers) and red crosses show outliers, which are defined as being outside of the range of 1.5 times the quartiles (approximately $\pm 2.7\sigma$). 113
Figure 4.3 Residuals of winter balance predicted using MLR for all density interpolation methods. 113

Figure 4.4 Summary of residuals from estimated winter balance values found using MLR coefficients (S4). Red line indicates median, blue box shows first quantiles, bars indicate minimum and maximum values (excluding outliers) and red crosses show outliers, which are defined as being outside of the range of 1.5 times the quartiles (approximately $\pm 2.7\sigma$). 114
Figure 4.5 Map of the residuals from estimated winter balance values found using MLR coefficients (S4) for each measurement location. 114
Figure 4.6 Boxplot showing the range of regressor coefficients that are estimated with winter balance values calculated using all density assignment methods. Topographic parameters are distance from centreline (d_C), elevation (z), aspect (α), slope (m), northness (N), curvature (κ) and wind redistribution (Sx). Within each box, the mean is shown as a circle, the median as a horizontal line, the interquartile range (IQR) as a coloured box, two times the IQR as dashed lines beyond the box and outliers as single points. 115
Figure 4.7 Boxplot showing the range of semi-partial correlation that are estimated with winter balance values calculated using all density assignment methods. Topographic parameters are distance from centreline (d_C), elevation (z), aspect (α), slope (m), northness (N), curvature (κ) and wind redistribution (Sx). Within each box, the mean is shown as a circle, the median as a horizontal line, the interquartile range (IQR) as a coloured box, two times the IQR as dashed lines beyond the box and outliers as single points. 116
Figure 4.8 Modelled winter balance using coefficients determined using MLR and density assigned by inverse-distance weighting from snow pits (S4). Observed winter balance values are overlain on the maps. . . 117
Figure 4.9 Map of the difference between maximum and minimum winter balance estimated with MLR. Winter balance data is calculated with each density assignment method. Arrows indicate glacier flow direction and black dots show snow depth sampling locations. 117
Figure 4.10 Map of the difference between maximum and minimum winter balance (WB) values, expressed as a percent of the maximum WB, estimated with MLR and WB data calculated with each density assignment method. The colours have been scaled to highlight differences in the main part of the glaciers. Values of 0% are found where the minimum estimated WB is 0 m w.e. Arrows indicate glacier flow direction and black dots show snow depth sampling locations. . . . 118

Figure 4.11 Map of modelled winter balance (WB) using the MLR coefficient values for all density assignment methods. Measured WB is plotted as overlain filled circles. Glacier flow directions are indicated by black arrows and mean estimated WB values for each glacier are shown. . 119

Figure 4.12 Uniform model prior for eight topographic regressors used in BMA. 120

Figure 4.13 Boxplot showing the range of BMA regressor coefficients that are estimated with winter balance values calculated using all density assignment methods. Topographic parameters are distance from centreline (d_C), elevation (z), aspect (α), slope (m), northness (N), curvature (κ) and wind redistribution (Sx). Within each box, the mean is shown as a circle, the median as a horizontal line, the interquartile range (IQR) as a coloured box, two times the IQR as dashed lines beyond the box and outliers as single points. 124

Figure 4.14 Boxplot showing the range of semi-partial correlation explained by topographic parameters from the BMA regression using each density assignment method of estimating winter balance (WB). Topographic parameters are distance from centreline (d_C), elevation (z), aspect (α), slope (m), northness (N), curvature (κ) and wind redistribution (Sx). Within each box, the mean is shown as a circle, the median as a horizontal line, the interquartile range (IQR) as a coloured box, two times the IQR as dashed lines beyond the box and outliers as single points. 125

Figure 4.15 Comparison of BMA predicted and observed winter balance (WB) for three study glaciers. The WB values were calculated inverse distance weighted snow pit densities (S4). 126

Figure 4.16 Plot of all linear fits between BMA modelled and observed winter balance (WB) using eight options for calculating density. Mean R^2 value is shown for each sub-plot and a reference 1:1 line is also provided. See Figure 4.15 for a plot of the data. 126

Figure 4.17 Modelled winter balance using coefficients determined using BMA and density interpolated with inverse-distance weighting from snow pits (S4). Observed winter balance values are overlain on the maps.Arrows indicate glacier flow direction and black dots show snow depth sampling locations. 127

Figure 4.18 Map of the difference between maximum and minimum winter balance values estimated with BMA and winter balance data calculated with each density assignment method. Arrows indicate glacier flow direction and black dots show snow depth sampling locations. . . . 127

Figure 4.19 Map of the difference between maximum and minimum winter balance (WB) values, expressed as a percent of the mean WB, estimated with BMA and WB data calculated with each density assignment method. The colours have been scaled to highlight difference in the main part of the glaciers. Arrows indicate glacier flow direction and black dots show snow depth sampling locations. 128

Figure 4.20 Summary of estimated winter balance values found using BMA coefficients (S4). Red line indicates median, blue box shows first quantiles, bars indicate minimum and maximum values (excluding outliers) and red crosses show outliers, which are defined as being outside of the range of 1.5 times the quartiles (approximately ±2.7σ). . . 128

Figure 4.21 Residuals of winter balance predicted using BMA for all options of estimating density. 129

Figure 4.22 Summary of residuals from estimated winter balance values found using BMA coefficients (S4). Red line indicates median, blue box shows first quantiles, bars indicate minimum and maximum values (excluding outliers) and red crosses show outliers, which are defined as being outside of the range of 1.5 times the quartiles (approximately ±2.7σ). 129

Figure 4.23 Map of the residuals from estimated winter balance values found using BMA coefficients (S4) for each measurement location. 130

Figure 4.24 Map of modelled winter balance using the BMS coefficient values for all density assignment methods. Measured winter balance is plotted as overlain filled circles. 131

Figure 4.25 Boxplot showing the range of values of coefficients for each topographic parameter from both MLR and BMA analysis for Glacier 4 (left), Glacier 2 (middle) and Glacier 13 (right). Note the different y axes for the three glaciers. Topographic parameters are distance from centreline (d_C), elevation (z), aspect (α), slope (m), northness (N), curvature (κ) and wind redistribution (Sx). Within each box, the mean is shown as a circle, the median as a horizontal line, the interquartile range (IQR) as a coloured box, two times the IQR as dashed lines beyond the box and outliers as single points. 132

Figure 4.26 (a) Mean winter balance and (b) elevation regression coefficient found with varying number of runs in the cross validation algorithm. . . 134

Figure 4.27 Spatial distribution of winter balance (WB) estimated using simple kriging with densities assigned as per S2 (Table 2.5). Locations of snow-depth measurements are shown as black dots. Ice-flow directions are indicated by arrows. Values of glacier-wide WB are given below labels. 136

Figure 4.28 Comparison of estimated (simple kriging) and observed winter balance (WB) for three study glaciers. The WB values were calculated using inverse-distance weighted snow pit densities (S4). 138

Figure 4.29 Simple-kriging winter-balance confidence interval (95%) as a percent of distributed WB, found using kriging. The WB value were estimated using density S4. Arrows indicate glacier flow direction and black dots show snow depth sampling locations. 138

Figure 4.30 Distributed BMA residuals estimated by regression kriging. Arrows indicate glacier flow direction and black dots show snow depth sampling locations. Dashed line indicates approximate ELA. 141

Figure 4.31 Winter balance estimated by adding kriged regression residuals to winter balance estimated using topographic regression with BMA. Observed winter balance values are overlain on the maps. Arrows indicate glacier flow direction. 141

Figure 4.32 Comparison of estimated (regression kriging) and observed winter balance (WB) for three study glaciers. The WB values are calculated using inverse-distance weighted snow pit densities (S4). 142

Figure 4.33 Mean observed winter balance and estimated winter balance using topographic regression (LR), simple kriging (SK) and regression kriging (RK), averaged over density assignment methods. 142

Figure 4.34 Mean correlation coefficient (R^2) between observed winter balance and estimated winter balance using topographic regression (LR), simple kriging (SK) and regression kriging (RK) at sampling locations, averaged over all density assignment methods. 143

Figure 4.35 Mean WB and mean estimated winter balance using topographic regression, kriging and regression kriging. 144

Figure 4.36 Correlation coefficient (R^2) between observed WB and mean estimated winter balance using topographic regression, kriging and regression kriging at sampling locations. 144

Figure 5.1 Distributions of glacier-wide winter balance (WB) for Glaciers 4 (G4), 2 (G2) and 13 (G13) that arise from various sources of uncertainty. WB distribution arising from grid-scale uncertainty (σ_{GS}) (left column). WB distribution arising from interpolation uncertainty (σ_{INT}) (middle column). WB distribution arising from a combination of σ_{GS}, σ_{INT} and density assignment uncertainty (σ_{ρ}) (right column). Results are shown for interpolation by linear regression (LR, top row) and simple kriging (SK, bottom row). Left two columns include eight distributions per glacier (colour) and each corresponds to a density assignment method (S1–S4 and F1–F4). . 150

Figure 5.2 Relative uncertainty in distributed winter balance (WB) found using linear regression (top row) and simple kriging (bottom row). Values closer to one indicate higher relative uncertainty. Ice-flow directions are indicated by arrows. 151

Figure 6.1 Transfer of regression coefficients to estimate distributed winter balance on study glaciers. winter balance found using Glacier 4 (top), Glacier 2 (middle) and Glacier 13 (bottom) regression coefficients. The mean WB from all density interpolation options is shown. Arrows indicate glacier flow direction. 156

Figure 6.2 Root mean squared error (RMSE) at sampling locations when regression coefficients are transfered between glaciers. The mean RMSE from all density assignment options is shown. 157

Figure 6.3 Winter balance (WB) estimated using transferred regression coefficients from each glacier. (Top row) Glacier 4 regression coefficients applied to all glaciers. (Middle row) Glacier 2 regression coefficients applied to all glaciers. (Bottom row) Glacier 13 regression coefficients applied to all glaciers. The glacier-wide WB is also shown. Arrows indicate glacier flow direction. 157

Figure 6.4 Relationship between winter balance (WB) and linear distance from the regional topographic divide between the Kaskawulsh and Hubbard Glaciers in the St. Elias Mountains. Point-scale values of WB from snow-pit data reported by Taylor-Barge (1969) (blue boxes, P-WB). LR-estimated glacier-wide WB calculated using density assignment S2 for Glaciers 4 (G4), 2 (G2) and 13 (G13) with errors bars calculated as the standard deviation of Monte Carlo-derived WB distributions (this study) (open orange circles, G-WB). Point-scale WB estimated from snow-pit data at two locations in the accumulation area of the Kaskawulsh Glacier, collected in May 2016 (unpublished data, SFU Glaciology Group) (filled orange dots, P-WB). Black line indicates best fit ($R^2 = 0.85$). 158

Chapter 1

Introduction

Snow accumulation, as the dominant input of mass to alpine glaciers, plays an important role in governing their mass balance and the hydrology of alpine catchments ~~more broadly~~. This has implications not only for the availability of water for local ecological and human use (Barnett and others, 2005; O'Neel and others, 2014), but also for rates of global sea-level rise (Gardner and others, 2013). It is therefore necessary to understand the spatial distribution of snow on glaciers. However, achieving such an understanding is complicated by the fact that snow distribution in alpine regions is not uniform or static, but rather highly variable and influenced by diverse and dynamic processes operating on multiple spatial and temporal scales. Although previous research has attempted to account for these processes through the development of various techniques of measurement and modelling, little is known about how they operate in glacierized alpine environments. This severely limits possibilities of quantifying and predicting snow distribution on glaciers, particularly in remote locations where frequent empirical measurements are difficult (Nolan and others, 2015).

Chapter 1 examines what is currently known and unknown about the topic of snow accumulation on glaciers and its spatial variability. Section 1.1 begins with an overview of accumulation variability within alpine regions in general, as there is a considerably greater breadth of studies devoted to snow in ~~non-~~glacierized alpine basins. Section 1.2 reviews different ways of modelling the distribution of snow in alpine environments, while Section 1.3 describes methods for measuring accumulation and their relative merits and challenges. Section 1.4 compiles studies that specifically ~~look at~~ accumulation variability on glaciers and summarizes their key findings. Section 1.5 focuses on mass balance and snow distribution research conducted the St. Elias Mountains, a large glacierized region where little is known about snow distribution and its effects on glacier mass balance. I then identify significant gaps that currently exist in the literature. In Section 1.6 I present an overview of the research scope of this study.

1.1 Accumulation variability

The spatial distribution of seasonal snow accumulation can vary significantly. This is a result of interactions between spatially and temporally variable atmospheric conditions and heterogeneous topography (Deems and Painter, 2006; Liston and Elder, 2006). Understanding and predicting snow distribution therefore requires accounting for factors that include atmospheric circulation, precipitable water, air pressure, air temperature, wind speed and direction, elevation, slope exposure, presence of orographic barriers, surface slope and aspect, surface roughness and relief (Schweizer and others, 2008b; McGrath and others, 2015).

1.1.1 Topographic scales

Snow accumulation is spatially variable on point scales (<5 m), hillslope scales (1–100 m), watershed scales (100–10,000 m) and regional scales (10–1000 km) (Clark and others, 2011). The features and conditions that lead to variability at these scales differ (see Table 1.1) and their relative importance depends on the topography and climate of the study area. Inclusion of parameters that describe relevant processes at multiple scales has been shown to improve models that aim to explain measured snow distribution (Marchand and Killingtveit, 2005; Clark and others, 2011).

Point-scale variability is generally associated with surface roughness effects and the presence of small obstacles. These effects can be significant in vegetated landscapes or when the surface is very rough (e.g. boulder field) (López-Moreno and others, 2011). Many parts of a glacier ~~though~~ are characterized by a relatively smooth surface, with roughness lengths on the order of centimetres (Hock, 2005). In these areas, point-scale variability of snow depth is low. However, in heavily crevassed regions, point-scale variability can be large and thus have a significant impact on snow distribution in the area (McGrath and others, 2015).

Hillslope-scale variability is caused by variations in the surface topography of the glacier. The curvature and slope of the surface as well as the presence of local ridges or depressions can affect where snow is located (Blöschl, 1999; Sold and others, 2013). Avalanching can also redistribute snow, especially on the margins of a glacier (Blöschl and others, 1991; Mott and others, 2008).

Watershed-scale variability results mainly from interaction between changing elevation and aspect with a basin and the atmospheric conditions (Clark and others, 2011). In particular, orographic lifting and shading can result in higher elevation and north-facing areas of the glacier having more snow than other areas (Mott and others, 2008; Sold and others, 2013). Gradients in temperature from elevation changes also affect the freezing level, which determines whether precipitation falls as snow or rain (Blöschl and others, 1991).

Regional-scale variability occurs when areas within a mountain range have differing amounts of snow. Often, this results from horizontal precipitation gradients and rain shad-

Table 1.1: Relevant spatial scales for snow variability on glaciers. Information from Clark and others (2011).

Scale	**Length**	**Associated glacier feature**
Point	<5 m	Crevasses
Hillslope	1–100 m	Local surface topography (curvature, slope), avalanching
Watershed	100–10,000 m	Elevation, aspect
Regional	10–1000 km	Horizontal precipitation gradient across mountain range

ows forming on the lee side of topographic divides. Areas with large, steep mountains are especially affected by these processes.

Generally, spatial variability increases with spatial scale (Clark and others, 2011). Extent and spacing of measurements must therefore capture variability both across the study area and at smaller scales. Clark and others (2011) note that studies of snow water equivalent (SWE) that have been conducted in alpine environments vary considerably in the extent and spacing of their measurements.

1.1.2 Snow drift and preferential deposition

Snow drift and preferential deposition are crucial factors that influence the distribution of snow (Lehning and others, 2008; Winstral and others, 2002; Clark and others, 2011). Sharp changes in topography create convergent and divergent airflows close to the surface, leading to turbulence and vorticity. This terrain-induced turbulence modifies mean wind (and snow particle) velocities, and can thus influence snow distribution (Mott and others, 2008; Lehning and others, 2008; Dadić and others, 2010).

Snow drift is the erosion and deposition of ~~already~~ deposited snow (Dadić and others, 2010). In general, erosion on the windward side is caused by increased wind speeds and deposition on the lee side of ridges is due to decreased wind speeds (Liston and Sturm, 1998; Mott and others, 2008; Dadić and others, 2010). Mott and others (2010) found that creep, which is the rolling of snow particles on the snow surface, and saltation, which is the bouncing and dislodging of snow particles, are primarily responsible for the formation of cornice-like features.

Preferential deposition is inhomogeneous precipitation in the absence of local erosion (Lehning and others, 2008). It is mainly governed by winds, where higher wind velocities and updrafts on the windward side of ridges cause reduced deposition while reduced wind velocities on the lee side enhance deposition. This process can occur at relatively low wind speeds because it does not require the lifting of already deposited snow—instead, it only needs to act with or against the falling snow (Mott and others, 2008; Dadić and others, 2010). For example, Mott and others (2011) found that the spatial structure of snow distribution in an alpine bowl was dominated by the preferential deposition of precipitation due to altered air flow fields.

Both snow drift and preferential deposition can occur at multiple spatial scales. Enhanced accumulation has been observed at the point scale in small depressions and near obstacles, at the hillslope scale along ridges and at the watershed scale in areas with sheltered aspects (Harrison, 1986; Blöschl and Kirnbauer, 1992; Mott and others, 2008; Winstral and others, 2002; Clark and others, 2011).

1.2 Snow distribution models

The distribution and variability of snow distribution can be estimated using either dynamic or statistical models. These models help to determine relevant processes that affect accumulation, generally by relating its spatial distribution to meteorological and topographic descriptors. Inferences made from these models drive the direction of future studies and provide valuable insight into understanding how snow variability arises. Accounting for wind in snow distribution models is especially important because it plays a dominant role in spatial patterns of accumulation (Winstral and others, 2013).

1.2.1 Dynamic models

Deposition and redistribution of snow can be represented using physically based, spatially distributed models. The general aim of these models is to simulate surface processes and how they vary spatially and temporally (Mott and others, 2008). These models usually consider atmospheric conditions including freezing level, precipitation rates, relative humidity and wind speed and direction, as well as processes such as orographic lifting, cloud formation, downslope evaporation, advection and fallout, snow metamorphism and wind redistribution of snow (erosion, saltation) due to terrain induced turbulence (Smith and Barstad, 2004; Liston and Elder, 2006; Lehning and others, 2008; Mott and others, 2008). Modelling the dynamically induced flows of these components together describes the preferential deposition and redistribution of snow in alpine environments (Lehning and others, 2008; Mott and others, 2008; Dadić and others, 2010).

Many models have been developed to describe preferential deposition and redistribution. Early models were developed for flat or gently rolling terrain where boundary layer flow is better understood (Dadić and others, 2010). Boundary layer flow in steep terrain is generally non-linear (Mott and others, 2008; Dadić and others, 2010), so a number of different approaches have been applied. For example, Dadić and others (2010) and (Lehning and others, 2008)modelled wind-flow velocities by solving non-hydrostatic, compressible Navier-Stokes equations in 3-D and aimed to conserve momentum, heat, mass and states of water. Smith and Barstad (2004) employed Fourier transforms in a linear orographic model, which allowed for a more accurate representation of complex terrain.

Dynamic models are a valuable way to determine accumulation variability. Since they use physically consistent processes, they can be applied to any site. Dynamic models can also be used in different climatic conditions meaning that they can be applied to past and projected accumulation regimes (Clark and others, 2011). ~~Furthermore, a historic data set of variables is not needed to generate meaningful output.~~ Another advantage of dynamic models is that they allow for high temporal resolution (e.g. Mott and others (2008) have a 1 hour time step), which allows for snowpack evolution to be examined.

Application of dynamic models is however operationally complex and computationally expensive, and also requires a diverse set of observations. A large number of input parameters, such as precipitation, wind speed and direction, air temperature and relative humidity, need to be measured frequently and extensive sampling within a study region is required for accurate modelling(Liston and Elder, 2006). For example, Dadić and others (2010) used meteorological data from three automatic weather stations located throughout the study basin, while in the study done by Mott and others (2008) monthly stake measurements were needed. Such a well-monitored basin can be difficult to achieve in remote or inaccessible areas. A number of other dynamic models, such as those described in Fowler and others (2007), use general circulation model values to drive local circulation models, but model output strongly depends on model boundary choice. Even with sufficient and appropriate input data, the models must assume a number of parameters and simplify parameter relationships (e.g. constant mean wind speed (Mott and others, 2008)) to characterize the atmosphere, which may not realistically describe air movement and stability. Additionally, the models do not account for all modes of snow transport. For example, snow deposition due to avalanching can be an important process of snow transport that is not captured in current models (Mott and others, 2008).

1.2.2 Statistical models

Statistical models of snow variability establish empirical relationships between snow distribution and external variables (Fowler and others, 2007). These models assume that local distribution is forced by external factors, such a meteorological conditions or topography, which can be described by proxy parameters.

Statistical downscaling

Statistical downscaling is the process of determining an empirical relationship between large-scale atmospheric conditions and regional climates (Fowler and others, 2007). In general, this relationship is expressed as a function F such that regional variables R are found by $R = F(X)$ where X encompasses large-scale climate variables (Fowler and others, 2007). These models are trained and validated using gridded reanalysis data from global climate models (X) and point observations (R). Performance of these models is measured using correlation coefficients, distance measures (e.g. root mean squared error)~~,~~ or explained variance (Fowler and others, 2007).

There are three main types of statistical models (Fowler and others, 2007). The first is a regression model, which directly quantifies a relationship between a local variable and a number of large-scale variables. Statistical methods such as multiple linear regressions (Hanssen-Bauer and Førland, 1998), principal component analysis (Kidson and Thompson, 1998), canonical-correlation analysis (Busuioc and others, 2001), neural networks (Zorita and Von Storch, 1999) and singular value decomposition (Widmann and others, 2003) can be employed. The second type of model is a weather typing scheme, which relates the occurrence of a particular 'weather class' to local variables. Weather classes can be found using empirical orthogonal functions or cluster analysis (Fowler and others, 2007). The third model uses weather generators that simulate local precipitation using a prescribed distribution of precipitation (Fowler and others, 2007).

Large-scale input variables that are usually chosen (e.g. sea-level pressure, geopotential heights) for statistical downscaling are representative of large-scale circulation. Increasingly, other variables such as humidity are being incorporated into analyses to account for mechanisms that rely on thermodynamics and vapour content (Fowler and others, 2007). When focusing on precipitation, integrated vapour transport (IVT) can be used as a proxy for precipitable water in the atmosphere and can be used to identify corridors of large water vapour transport that correlate with intense precipitation events (Neiman and others, 2008).

Statistical models are a simple way to examine variability. They are computationally efficient and comparatively easy to apply because they are based on standard and accepted statistical procedures (Fowler and others, 2007). Furthermore, predicting variables does not require prior knowledge of all the processes that affect the variable. Functions can therefore be ~~calculated~~ for situations where all processes are currently not accounted for or where many processes are equally important.

Although the application of statistical downscaling is simple, it has a number of disadvantages. The method is difficult to apply in areas that have minimal historical data, as model performance is better when a long and reliable data set is used for calibration (Fowler and others, 2007). Statistical downscaling also assumes that the relationship between large-scale and local variables is stationary in time, limiting the ability of models to project into the future (Fowler and others, 2007). Furthermore, an empirical relationship assumes that there is no climate system feedback and the data generated through the empirical function are subject to the same biases as those of the original data set (Fowler and others, 2007). Wilby and Wigley (2000) also note~~s~~ that the choice of large-scale variable domain (location and spatial extent) exerts a strong ~~effect~~ on the accuracy of the empirical function.

Terrain-based parametrization

Terrain-based parametrization determines empirical relationships between topographic indices and observed data. To determine topographic indices, the terrain in the study area is divided into gridcells where terrain parameters (e.g. slope, curvature, aspect, "northness", wind exposure, topographic similarity) are calculated (Anderson and others, 2014; McGrath and others, 2015). The variable of interest is then measured in the study area and a relationship between grid-cell terrain parameters and observed data can be established (e.g. Blöschl and others, 1991; Liston and Sturm, 1998; Anderton and others, 2004; McGrath and others, 2015).

Terrain-based parametrization requires a good terrain model and a meaningful network of observed data. For example, Molotch and others (2005) found that that there were significant differences in modelled snow distribution when different terrain models were used. This is likely because the terrain-model grid size affects the value of the calculated terrain parameter for the cell. Terrain-based parameterization also requires sufficiently high resolution and spatial extent of observed data. When measuring accumulation, the variability within the study area ~~needs~~ to be captured and all areas should be well represented.

Relating terrain model parameters ~~with~~ observed data is often accomplished with simple statistical methods. Multiple linear regressions (Marchand and Killingtveit, 2005; Sold and others, 2013; McGrath and others, 2015), mixed-effects multiple regression (Kasurak and others, 2011), parametric probability distributions (Clark and others, 2011), bivariate screening (Anderton and others, 2004), probability distribution functions (Kerr and others, 2013) and regression tree models (Elder and others, 1998; Winstral and others, 2002; Molotch and others, 2005; Revuelto and others, 2014; Wetlaufer and others, 2016) are among the more popular models. These models relate snow distribution to terrain parameters with varying success. For example, the multiple linear regression model developed by Sold and others (2013) explained about 50% of the variance of snow depth while the model developed by Anderton and others (2004) explained 70–80% of the variance in snow water equivalent. A number of studies have found that elevation and wind redistribution parameters explain ~~the majority~~ of the variance in observed snow depth or snow water equivalence (e.g. Erickson and others, 2005; Trujillo and others, 2009; Schirmer and others, 2011; Grünewald and others, 2014; McGrath and others, 2015). Interaction parameters (e.g. $slope \times orientation$) have also been found to be significant predictors ~~for~~ precipitation distribution in alpine areas (Basist and others, 1994). Erxleben and others (2002) and Molotch and others (2005) note that many relationships between accumulation and controlling parameters are nonlinear so use of regression tree models yields better results. Combining statistical models has also been seen to improve model accuracy. Examples include combining linear regressions with generalized additive models (López-Moreno and Nogués-Bravo, 2006) as well as binary decision trees with kriging (Balk and Elder, 2000).

Relating topographic parameters and observed data is a simple approach to understanding processes that affect variability. Although no physically-based relations are employed, terrain parameters can act as proxies for processes that are known to occur (McGrath and others, 2015). In this way, dominant processes can be inferred through ~~easy to find~~ statistical relationships. This approach is especially powerful in alpine environments, where topography strongly affects local snow distribution.

While terrain-based parametrization is easy to employ, its usefulness in understanding now distribution can be limited. This method assumes that variability between cells is larger than ~~within cell variability,~~ which may not necessarily apply to all cells, especially in steep terrain or where grid size is comparatively large. Marchand and Killingtveit (2005) found that the standard deviation within the 30 m by 30 m gridcells used in ~~the~~ study was slightly larger than the between-grid variability. Additionally, Grünewald and others (2013) observed that local statistical models are able to perform well but that they cannot be transferred to different regions and that regional-scale models are not able to explain ~~the majority of~~ variance. The temporal transferability of terrain-based parameterization is also not reliable. Grünewald and others (2013) found that local models could be applied between years while Revuelto and others (2014) found that snow distribution variability could not be explained by their model in low snow years. Furthermore, the use of terrain parameters as proxies does not provide meaningful insight into relevant processes. This is important when attempting to predict distribution of variables in a different climate or location.

1.3 Measuring accumulation

Estimating accumulation requires snow density and depth measurements. Measuring these ~~parameters~~ within a glacierized basin has many challenges. Basin location and topography affect accessibility, while the cost and time required to conduct measurements can be prohibitive. In most cases, the resolution of measurements over a large area is insufficient to approximate the true variability (Blöschl, 1999; Deems and others, 2006).

Snow density can be measured directly or with models of snow density change. To measure bulk density, a column of snow with a known volume is excavated (in a snow pit or with a ~~firn corer~~) and weighed (Sold and others, 2013, 2014). Usually, a number of snow-column densities are measured and the average density is taken as representative of glacier-wide density (e.g. Machguth and others, 2006; Grünewald and others, 2010; McGrath and others, 2015). This can result in error when calculating snow water equivalence (SWE) because density can vary spatially and temporally (due to total snow depth, elevation, solar radiation and wind effects) in a way that is not captured by a limited number of snow density measurements (Grünewald and others, 2010; Wetlaufer and others, 2016). However, snow density has been seen to vary over greater spatial scales than snow depth so fewer density measurements than depth measurements are usually made (Elder and others, 1998; Clark and others, 2011). Snow and firn density can also be calculated using models that account for ~~relevant~~ processes such as compaction from overl~~a~~ying snow and refreezing of meltwater

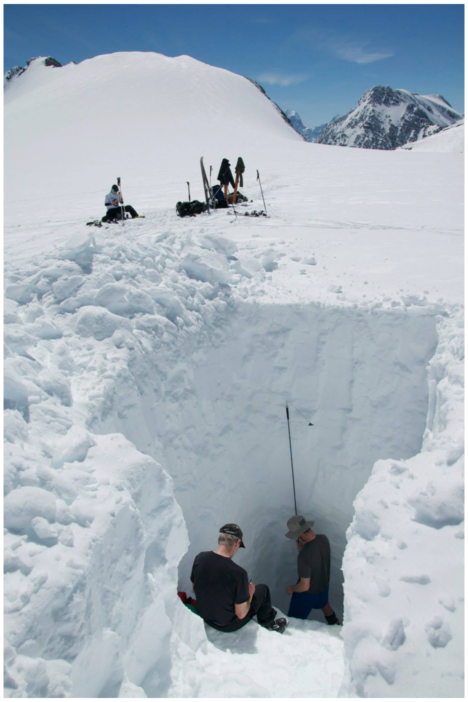

Figure 1.1: Digging a snow pit in the accumulation area of Haig Glacier, Rocky Mountains

(Herron and Langway Jr, 1980; Sold and others, 2014). Densification processes are difficult to capture in models ~~though,~~ so they should be applied with caution (Mellor, 1974).

Three main methods are currently used to measure snow depth. Probing involves taking *in situ* point measurements of snow depth, ground-penetrating radar (GPR) surveying involves using radar to detect the snow depth along continuous lines and digital elevation model (DEM) subtraction involves taking the difference between the glacier surface at the end of the ablation and end of the accumulation seasons to find snow depth. Methods are selectively applied based on desired spatial resolution, cost effectiveness and equipment availability. Each is prone to different sources of error and there is ongoing research to reconcile these approaches (Sold and others, 2014).

1.3.1 Snow probing

Measurement

The most direct way of measuring snow depth is by probing. To determine the snowpack thickness, the height of the snow above the end of the previous year's ablation surface is measured. Usually, a number of snow height measurements are obtained close to each other and the mean value is taken to be representative of that location. For example, Machguth and others (2006) took the mean of nine snow probe measurements within a 7 m radius as representative of a measurement location.

In the ablation zone, snow depth is easy to measure because the interface between the end-of-summer melt surface and the ~~beginning of~~ winter accumulation is well defined (i.e. glacier ice) (McGrath and others, 2015). In the accumulation zone however, the snow surface at the end of the melt season may not be easily distinguishable from the winter accumulation (Grünewald and others, 2010). It is common for the accumulation zone to have a heterogeneous surface at the end of the melt season some areas do not experience any melt, while other areas experience some melt and the melt water percolates through the snow and firn. Melt water generated from warm weather or rain events, especially in the early and late parts of the accumulation season, can refreeze in the snowpack to form ice lenses (Sold and others, 2014). As a result, the interface can be difficult to ~~observe~~ and contain a combination of dense or compacted snow, ice lenses and/or firn. Probing in the accumulation zone can therefore result in erroneous depth measurements — penetration into the dense snow or firn will make it seem like a deeper snowpack exists and probing to an ice lens within the snowpack can make it seem like shallower snow is present (Sold and others, 2013). Snow pits and ~~firn~~ cores are therefore used to examine snow and firn layers and to determine where the current season's snow begins.

To determine the basin-wide snow distribution, point snow depth measurements from probing need to be interpolated and extrapolated. This is often done using a statistical regression on parameters such as slope, aspect, curvature and susceptibility to wind redistribution (e.g. Wheler and others, 2014; McGrath and others, 2015). A regression generates an equation that is site specific and is used to estimate accumulation for each gridcell based on the values of its topographic parameters.

Snow probing is the simplest and oldest method used to determine accumulation. At the most basic level, it requires little more than a probe to determine depth, a way to determine location (such as a hand-held GPS) and a shovel to dig snow pits (see Figure 1.1). Furthermore, this method directly measures snow depth so no data processing or corrections are needed and depth uncertainty is simple to quantify (often multiple depth measurements are taken close together) (Sold and others, 2013).

There are however many drawbacks to this method. *In situ* probing and digging snow pits is ~~incredibly~~ time-consuming (Deems and Painter, 2006). This limits the number of measurements that can be made, which means that accumulation distribution is underrepresented and spatial variability in accumulation is difficult to capture (Sold and others, 2014). Measurement is also limited to areas that are both accessible and safe for researchers. In complex terrain many areas cannot be surveyed, resulting in data gaps. Sold and others (2013) noted that this systematic bias can result in incorrect values of glacier-wide accumulation — particularly because inaccessible areas such as cliffs and ridges have relatively ~~shallow~~ accumulations (due to wind erosion), while heavily crevassed areas can accumulate deep snow packs.

Sampling Design

Optimal sampling schemes for snow probing are central ~~for~~ accurately estimating snow distribution and mass balance from *in situ* measurements. Measuring snow depth and travelling between measurement locations is both time consuming and can disturb the snow so care must be taken to choose a sampling scheme that avoids bias, allow for the greatest variability to be measured and minimizes distance travelled (Shea and Jamieson, 2010). A design that maximizes accuracy and minimizes effort is therefore desired (Elder and others, 1991) and both theoretical (Trujillo and Lehning, 2015) and applied (Kronholm and others, 2004; Shea and Jamieson, 2010) investigations of various sampling designs have been pursued. There are a number of different designs that have been employed to obtain point measurements, including pure random, linear random, nested, gridded random and gridded.

A purely random distribution of points is favourable because it avoids all bias, has the best correlation with true distribution and is likely to capture the most variability (Kronholm and Birkeland, 2007; Shea and Jamieson, 2010). Logistically ~~though,~~ it is difficult to successfully measure all points in the study area because some may be impossible to access and some may be disrupted during travel or measurement. ~~This~~ design often results in inefficient travelling routes, ~~which decreases~~ the number of possible point measurements. Elder and others (1991) show a simple basin-wide random sample is a less optimal sampling scheme than a stratified random sample that accounts for known variation. One ~~instance~~ of a purely random sampling scheme can be seen in Figure 1.2(a).

Linear-random sampling schemes impose a structure to traverse as much of the study area as possible but allow for a random distance between sampling points. An example of this scheme is the ‘star’, created by Shea and Jamieson (2010). A significant advantage of this scheme is that it was designed to minimize distance travelled while still measuring snow properties in various orientations and various distances apart, which reduces bias. However, since the observer travels in straight transects there is still a potential to miss smaller features or ones that parallel the transects (spatial autocorrelation). Shea and Jamieson (2010) used comparative Monte Carlo simulations to validate that the star scheme performs ~~equivalently~~ or better than other (more structured) sampling methods and that it converges to the true distribution as well as a purely random scheme. One ~~instance~~ of a linear-random sampling scheme can be seen in Figure 1.2(b). Linear-random sampling can also be done in an ‘hourglass’ shape with an inscribed circle (referred to as an hourglass sampling scheme). As seen in Figure 1.2(f), this pattern allows sampling in all directions and captures a wide range of snow depths from the underlying snow distribution (Parr, C., 2016 personal communication).

Gridded-random designs involve dividing the study area into equal sized areas and then sampling randomly within each area. The L-grid is an example of this scheme (Bellaire and Schweizer, 2008; Elder and others, 2009; Bellaire and Schweizer, 2011). In this scheme,

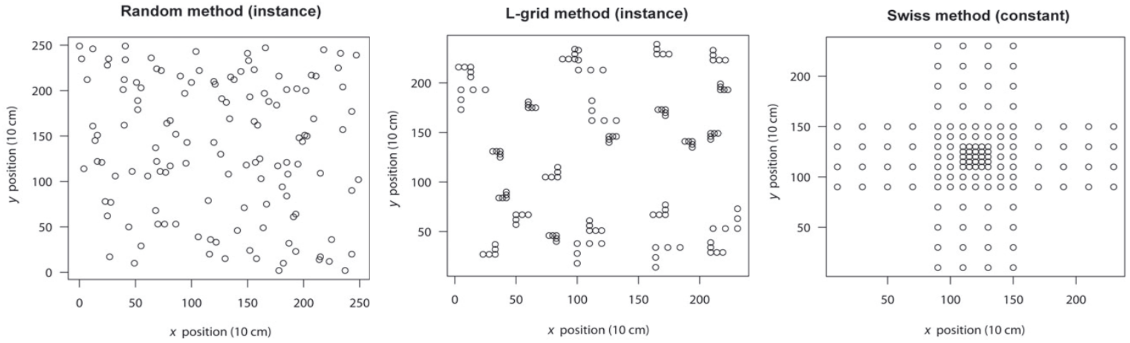

(a) Pure random **(c)** L-grid **(e)** Swiss grid

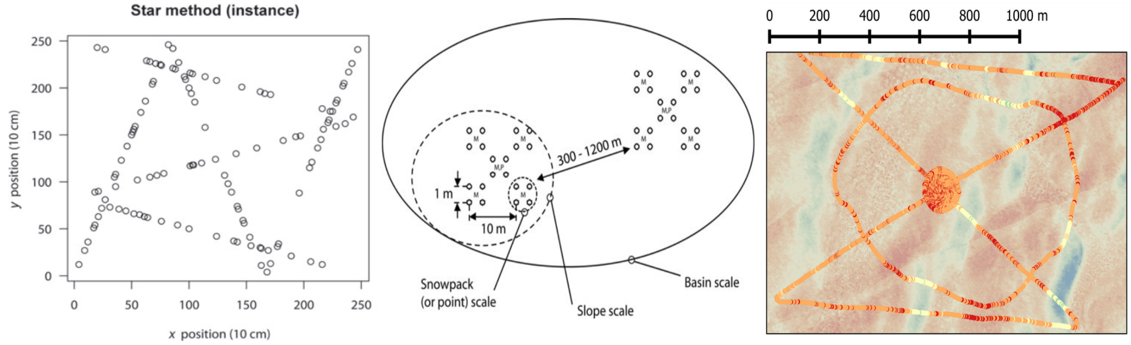
Star method (instance)
y position (10 cm)
x position (10 cm)
0
50
100
150
200
250
300 - 1200 m
1 m
10 m
M
M,P
Snowpack
(or point) scale
Slope scale
Basin scale
0
200
400
600
800
1000 m

(b) Star **(d)** Nested **(f)** Hourglass

Figure 1.2: Examples of snow sampling schemes. Figures (a), (b), (c) and (e) from Shea and Jamieson (2010). Figure (d) from Schweizer and others (2008a). Figure (f) from Parr, C., (2016 personal communication).

the study area is divided into a grid and in each cell a random location is chosen as the start of the transect. The cardinal direction and measurement spacing of the transect are chosen randomly. Transects consist of five measurements, with three in the first direction selected and two perpendicular to this, forming an 'L' shape. This scheme has a small error bias (maintains randomness), while allowing for more efficient measurement (Shea and Jamieson, 2010). Compared to the star scheme, the L-grid does not have a consistent travel distance and involves constant reorientation and finding of transect start locations, which decreases its efficiency. One ~~instance~~ of a gridded-random sampling scheme can be seen in Figure 1.2(c).

Nested sampling is a scheme that maintains a certain sampling pattern and applies it at various length scales. For example, Schweizer and others (2008a) took four point measurement in a 1 m square and did this 10 m apart to form another square. The set of measurements was then repeated 300–1200 m away to capture ~~basin scale values~~. Hierarchal trees that incorporate selected parameters are often used to determine nested sampling locations. Watson and others (2006) and Kasurak and others (2011) use hierarchal sampling to divide the study area into regions (often discontinuous) that are likely to have a similar snow distribution and low variance, which means they require fewer sampling locations. Nested sampling requires that the observer predetermine parameters that affect the spatial pattern of the variable. Often, remote sensing is used to obtain these parameters so the resolution of regions is limited to that of the remote sensing images (typically 30 m resolution). The variability that exists at scales less than the grid-size of the images is classified as being caused by 'random' effects, which are assumed to be unbiased and unpredictable (Watson and others, 2006). Nested sampling is well suited for regions with many complex and interacting parameters. For example, Watson and others (2006) used a hierarchal tree with time (traveling between locations), elevation, vegetation and solar radiation at various length scales to create subgroup to sample. ~~A nested sampling scheme can be seen in Figure 1.2(d).~~

Gridded sampling designs use regular measurement intervals in a grid pattern. Many variations of this scheme exist (Molotch and Bales, 2005; Kronholm and Birkeland, 2007; López-Moreno and others, 2011) with the most popular one being the Swiss cross (Kronholm and others, 2004). This nested arrangement allows for a larger area to be covered than a fully quadratic grid and measures at various spatial scales, leading to more reliable geospatial statistics. ~~This method allows for easy measurement and reveals details at various scales.~~ However, measurements are biased by regular spaced intervals and linear orientation, which could result in an under representation of the snow distribution further from the centre. A gridded sampling scheme can be seen in Figure 1.2(e).

1.3.2 GPR

Ground penetrating radar (GPR) can be used to find snow depth along continuous ~~lines.~~ This method is used to calculate the distance from the radar source to a boundary with a strong contrast in dielectric permittivity, which corresponds to a change in material properties (Sold and others, 2013). When the speed of the radar wave through the material is known, the travel time can be measured and from this the distance calculated. On a glacier, the radar wave is able to penetrate snow and ice at MHz frequencies and the strongest reflections arise when water is present (Sold and others, 2013). To measure snow depth, GPR units are mounted on aircraft~~s~~ or snowmobiles that then travel over snow covered areas (see Figure 1.3) (Machguth and others, 2006; McGrath and others, 2015). The resulting processed radargram (e.g. Figure 1.4) gives a ~~continuous~~ snow depth profile. Processing of the radargrams ~~involves~~ using tracking algorithms that are able to trace continuous layers. Interpolation between transects is then done to find the glacier-wide accumulation. McGrath and others (2015) describe this process in five steps: (i) acquisition of GPR and probing data (ground truthing), (ii) calculation of snow density and radar velocity, (iii) calculation of snow thickness and resulting snow water equivalent (SWE), (iv) application of a correction to measured accumulation based on ground truth data and (v) use of a multiple regression model to extrapolate SWE across the glacier. The extrapolation of SWE ~~can~~ also be done using an inverse approach with a coupled surface energy-balance snow model (van Pelt and others, 2014).

GPR is an effective tool for measuring accumulation. It provides continuous snow depth transects, which means that spatial variability is well represented along the radar lines. Surveys also need to be conducted only once to gain depth observations, which makes data collection fast and and reduces logistical efforts (Machguth and others, 2006). GPR snow depth estimates are not affected by glacier dynamics and the ability to fly over steep or inaccessible regions means that all areas of a glacier can be measured.

A large limitation of GPR is the difficultly of processing radargrams. Areas where the snow–ice boundary is not well defined (i.e. the accumulation area) lack clearly contrasted material properties, which can lead to misinterpretation of their internal layers (McGrath and others, 2015). In the ablation area, the presence of crevasses can also result in radargram misinterpretation (Machguth and others, 2006). Variation and uncertainty in radar wave speed due to differing snow density and liquid water content can also affect depth calculations (Sold and others, 2013). Often, wave speed is only measured in a few reference locations so changes in snow pack properties cannot be accounted for. Lastly, there is no universal procedure for processing GPR data. Selection of parameters and processing algorithms is dependent on available equipment, field conditions, survey design and intention (Sold and others, 2013), which hampers the reproducibility of surveys.

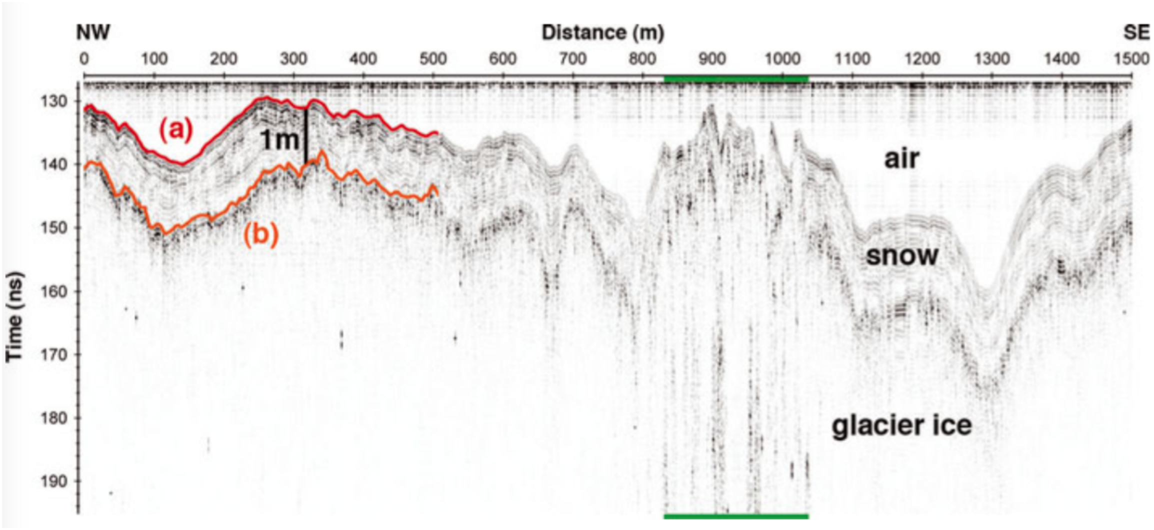

Figure 1.4: Radargram from the accumulation area of Findelengletscher, Valais, Switzerland. (a) The reflection at the air-snow interface. (b) The reflection at the snow-ice interface. Figure taken from Sold and others (2013).

1.3.3 DEM subtraction

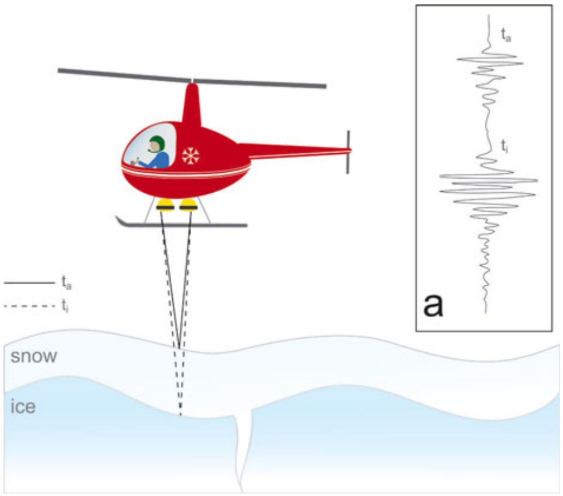

Figure 1.3: Schematic diagram of a helicopter-borne radar snow survey. The travel time for the signal to interact with the snow surface is shown as a solid line and the signal travel time of the interaction with the ice is shown as a dashed line. Together, these values can be used to determine snow depth. The inset (a) is an example waveform that would be recorded from these two events. Figure taken from Gusmeroli and others (2014).

Digital elevation model (DEM) subtraction involves taking two detailed surface topography scans — one at the end of the melt season and one at the end of the accumulation season — and subtracting them from each other to find the snowpack height. The largest advantage of this remote sensing method is that it provides a highly resolved spatial measurement of snow depth over an entire basin (Deems and Painter, 2006; Sold and others, 2013). Data collection is fast, although two surveys must be conducted. This technique is sensitive to other processes that change the glacier surface elevation, including vertical displacement due to ice flow (positive in the ablation area and negative in the accumulation area), firn compaction and surface lowering due to melt after the acquisition of the end-of-melt season DEM (Sold and others, 2013). For example, ~~(~~Sold and others, 2013) found that a first-order approach (where the observed elevation change was interpreted as snow accumulation) was inconsistent with snow depth probing — DEM subtraction showed decreasing accumulation with an increase in elevation. Corrections can be made to account for these discrepancies but they rely on *in situ* measurement of snow depth, knowledge of long-term mass balance, or information about the vertical displacement of ice from GPS ~~towers~~ (Sold and others, 2013).

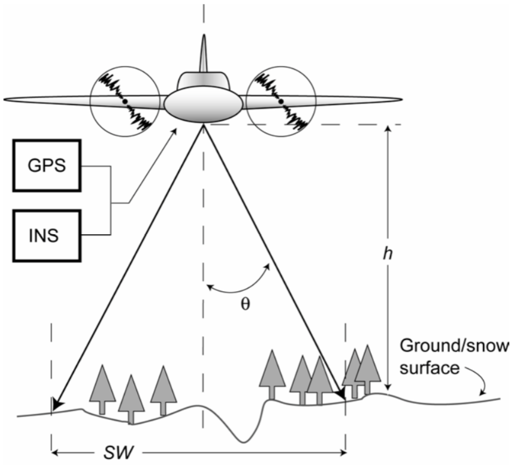

Figure 1.5: Schematic of airborne LiDAR system geometry. Scan angle (θ), height (h) and swath width (SW) are shown. Figure from Deems and Painter (2006).

Lidar and photogrammetry are the two main methods of producing DEMs. Lidar produces a surface elevation model by calculating the distance to a target (by measuring the time between an emitted and return laser signal) (Deems and Painter, 2006; Sold and others, 2013). Terrestrial lidar systems involve stationary units placed in vantage points from which they are able to scan the basin surface (Grünewald and others, 2010). Large basins require multiple overlapping scans to acquire a complete surface profile. Airborne lidar systems (see Figure 1.5) can also only scan a certain size footprint so the aircraft must fly over all parts of the basin to acquire a full surface profile. These systems also require an accurate global positioning system (GPS) — which is often corrected by referencing to a stationary GPS — to determine the 3D locations of the surface (Deems and Painter, 2006). Airborne systems are widely applied and favourable in large basins or ones where no vantage point exists ~~or is inaccessible~~. However, these systems are expensive so terrestrial scanners, which are comparatively more cost effective, are becoming popular (Grünewald and others, 2010).

Complex topography and multiple laser reflections can cause problems when producing a DEM from lidar data (Deems and Painter, 2006). Significant vertical changes result in

~~the~~ spreading of the laser footprint and an incorrect interpretation of distance. (Deems and Painter, 2006) shows that an error of 50 cm can result from lidar scans of 45° terrain from 1000 m flight height. Careful planning of flight paths can reduce this error. Scattering of laser light and penetration into the snow pack can also introduce error into height calculations, although its magnitude is small (∼cm) (Deems and Painter, 2006). When subtracting the two measured DEMs, misclassification of corresponding point locations can occur, resulting in error in the final accumulation value (Deems and Painter, 2006).

Photogrammetry uses photographs to produce a series of DEMs that can be subtracted to find snow depth. Early attempts in the 1960s ~~at applying~~ this technique in snow covered areas suffered from poor vertical resolution due to overexposed photographs and the necessity of manual differencing (Nolan and others, 2015). Modern photography equipment, GPS and software technology have allowed for an increase in accuracy and lowering of costs associated with photogrammetry (Nolan and others, 2015). Current photogrammetry software is able to determine a snow surface profile relative to stable, snow-free points within the mapped area (Farinotti and others, 2010). The ~~photos~~ collected for DEM creation can also be used to identify suspect changes in the snow pack (Nolan and others, 2015). Errors in photogrammetric measurements arise from sensor noise and poor lighting. Camera sensor noise is present in all digital photographs and its location changes from picture to picture. These erroneous pixels can be misinterpreted by the software as actual differences in height and thus lead to significant topographic noise, especially in steep mountainous terrain (Nolan and others, 2015). Additionally, having sufficient contrast in the photographed snow surface is critical for determining surface profile. Flat light conditions can reduce the resolution of the DEM or result in an absence of data in those parts of the photograph (Nolan and others, 2015). ~~These effects can be avoided by waiting for better lighting~~.

1.3.4 Comparison of methods

The three methods of measuring accumulation differ in the extent of spatial information, collection techniques, costs and processing needs. Spatial footprint is lowest for probing, which means that data must be interpolated. Although the actual measurement is simple and has relatively low uncertainty, the interpolation of points can lead to misrepresentation of spatial variability and significant errors that are difficult to quantify. GPR provides continuous snow depth profiles, but interpolation is still needed between lines. Further, significant errors can arise from misinterpretation of layers in radargrams. DEM differencing has the advantage of allowing for the measurement of surface topography across the whole basin, but error can result when glacier dynamics affect surface height changes.

Large differences in data collection time and cost also exist. Probing has low equipment costs but requires ~~a large amount of human hours~~ for ground-based measurements. GPR and DEM subtraction both require the use of aircraft~~s~~ and expensive electronic equipment. However, these methods require lower logistical effort and data collection occurs quickly.

The three methods also have different data processing requirements. Simple statistical relations can be used for interpolating accumulation found by probing. However, GPR and DEM subtraction both require specialized software and knowledge of image processing methods, ~~which increases the likelihood that misinterpretations of observations will occur~~. GPR has an advantage over DEM subtraction because it is not subject to elevation changes due to glacier dynamics and firn compaction. However, DEM subtraction has the advantage of more easily detecting the previous year's surface in the accumulation area and provides complete coverage of the study area (Sold and others, 2013).

In general, Machguth and others (2006) and Sold and others (2013) found good correlations between probing measurements, GPR and DEM subtraction. However, (Sold and others, 2013) found that the methods did not always corroborate each other, particularly in crevassed areas and marginal regions. In crevassed areas, accumulation has large variation on small scales. The footprint of the GPR was usually too large to detect changes in snow depth ~~and~~ the movement of crevasses with time affected the lidar-derived snow depth. Marginal regions were misrepresented in the probing-derived profile because measurement ~~was~~ often not ~~conducted~~ in these areas. This area also included the uppermost part of the glacier where wind erosion had a significant effect on accumulation.

Choice of measurement technique for a snow survey is therefore dependent on project specific needs. Resolution, cost and equipment availability need to be considered when selecting the most appropriate method. To reduce errors and misrepresentation of measurements, multiple methods can also be applied (Machguth and others, 2006).

1.3.5 Temporally resolved methods

Temporally resolved methods take continuous measurements to provide a time series of snow accumulation. Usually, these methods involve relatively few measurement locations so they do not represent spatial variability well. However, they are especially useful for identifying large snowfall events (rapid increases in accumulation) and wind erosion (gradual decreases in accumulation).

There are a number of methods of measuring accumulation with time. Snow depth sensors, such as the SR50, measure the time between emission and return of an ultrasonic pulse (Ryan and others, 2008). As snow accumulates, the distance between the sensor and the snow surface decreases. Snow pillows, which are large (3 m diameter) bladders filled with antifreeze solution, directly measure changes in snow water equivalent with time (Archer and Stewart, 1995). As snow accumulates on the pillow, the weight of the snow forces an equivalent amount of the solution from the pillow to a standpipe. The height of the solution in the pipe is then recorded. Another method for measuring snow depth involves using multipath modulation of GPS signals (Larson and others, 2009; McCreight and others, 2014). Multipath modulation involves isolating GPS signals that are reflected from horizonal, planar reflectors, such as a snow surface. The distance between the geodetic

GPS receivers and the reflection point will change during the accumulation season, thus recording changes in snow depth. This method allows for the measurement of average snow depth in a ∼1000 m^2 area around the antenna (McCreight and others, 2014).

1.4 Snow distribution on glaciers

While studies of snow distribution in alpine regions are plentiful (Clark and others, 2011, and sources within) there are comparatively few studies on the distribution of snow on glaciers. Although glaciers are often found in alpine environments, they present a different setting for accumulation. The freezing temperatures of glacier ice allow for snow to stick earlier than on the surrounding rocks, which can be above freezing especially in the early part of the accumulation season. Additionally, the surface of a glacier is often less steep than the surrounding peaks, which allows for snow to deposit more easily. The margin of the glacier can also accumulate snow from avalanches released from the surrounding ~~peaks~~ (Blöschl and others, 1991; Mott and others, 2008). Further, most glaciers do not support vegetation, which has significant effects on snow accumulation in many alpine basins (Pomeroy and others, 1999). Alford (1985) found that in open alpine areas with snow fields and small cirque glaciers there was a wide range of SWE values over a relatively small range of elevation, while in the montane areas there was a strong relationship between elevation and SWE where SWE values increased rapidly with elevation. Since few studies have been done on this topic, it is difficult to say whether snow distribution on glaciers is fundamentally different than that of an alpine basin. This lack of snow variability quantification points to a significant gap in the literature.

Winther and others (1998) conducted one of the first accumulation variability studies on a glacier. A GPR system was used to measure snow depth along three large transects on Spitsbergen, Svalbard. It was found that the accumulation-elevation gradients varied considerably and that regional variability was large, with almost 50% more accumulation on the eastern coast and a minimum in accumulation in the inland locations. A number of subsequent accumulation studies in Svalbard have since been conducted. Pälli and others (2002) used GPR along longitudinal profiles of Nordenskjöldbreen and found 40 – 60% spatial variability over short distances. Grabiec and others (2011) compared snow distribution on four types of glaciers in Svalbard. It was observed that the land-terminating mountain glacier had a simple altitudinal gradient while the outlet glacier had a much weaker correlation and more wind-redistributed snow. It was thought that the orientation and shape of the glacier also had a significant impact on snow accumulation, with the glaciers that were oriented parallel to the dominant wind direction having stronger altitudinal gradients. Another glacier that was observed had no altitudinal gradient, so its distribution was determined by complex local conditions. The ice cap that Grabiec and others (2011) studied had all of these types of distributions in different areas.

Machguth and others (2006) conducted an airborne GRP survey of two adjacent glaciers in Switzerland. The lower part of the larger valley glacier showed a clear correlation between altitude and snow accumulation. The upper part of the glacier and the adjacent smaller glacier had no altitudinal trend and the fluctuations in depth were large. Additionally, the accumulation was 40% lower on the smaller glacier. The altitudinal trend is a well documented pattern and was thought to be a result of melt that occurred during warmer weather, which is more pronounced at lower elevations. Spatial variability of precipitation and redistribution of snow were believed to have resulted in the high spatial variability in higher parts of the study area. Since the majority of the precipitation events originated from one direction and the large glacier was on the lee side of a ridge, it experienced preferential deposition. Meanwhile, the smaller glacier was further along the storm track so it received less precipitation. Overall, Machguth and others (2006) showed that snow distribution on glaciers is not simply a function of altitude, which corroborated research done in other alpine catchments.

The most recent and comprehensive study of snow distribution on glaciers was done by McGrath and others (2015). This study focused on seven Alaskan glaciers of various sizes, orientations and distances from the Pacific Ocean. McGrath and others (2015) found that SWE was highly variable (40% differences) at the hillslope-scale and was especially large in the ablation area (which has a rough surface due to the presence of crevasses). The dominant control on SWE distribution was altitude, but multiple terrain parameters were needed to capture most of the variance — after elevation, wind exposure explained the most variance. McGrath and others (2015) also ~~plotted mean SWE difference against distance and~~ found that four of the study glaciers exhibited a rapid increase in variability over the first ∼150 m and a slow increase in variability beyond but the three other study glaciers exhibited a gradual increase in variability over the entire range. Although this was not a detailed investigation of observed length scales, it potentially points to a heterogenous nature of snow distribution length scales on glaciers ~~and the need for their increased measurement~~.

The study done by Walmsley (2015) contains the longest record of spatial distribution of snow accumulation. Walmsley (2015) analyzed 48 and 44 year records of two Norwegian glaciers for inter-annual stability in distribution patterns. It was found that snow accumulation is spatially heterogeneous yet it exhibits robust time stability in distributions. Reliability maps were then used to reduce the sampling scheme to one index site as well as a transect with 50 m elevation intervals for each glacier. Although winter balance reconstructions produced values within 0.15 m water equivalent, it was determined that a centreline transect underestimated winter balance. Transverse transects were therefore recommend as an addition to the sampling scheme to improve reliability. Additionally, several strongly irregular snow spatial distribution years were identified, which were inconsistent with the overall reduced sampling schemes.

The majority of studies that have examined snow distribution on glaciers have been done with either airborne or ground-based radar (e.g. Winther and others, 1998; Machguth and others, 2006; Grabiec and others, 2011; van Pelt and others, 2014; McGrath and others, 2015). In general, the radargrams provided valuable information but ground truthing by probing was always conducted. Gusmeroli and others (2014) also did a small GPR survey on an Alaskan glacier and found that GPR reflections were difficult to identify in areas of the glacier that had high debris content on the surface or in the upper part of the accumulation area. Sold and others (2013) did an extensive study that compared snow distribution values obtained by using probing, GPR and DEM subtraction with lidar. All three methods showed an overall altitudinal trend but with significant small-scale variability (for a comparison of the three methods and their relative benefits, see Section 1.3.4). van Pelt and others (2014) used GPR and a surface-energy balance model coupled with a snow model to examine accumulation variability. It was found that terrain parameters such as slope and curvature were good ~~representations~~ of preferential deposition. Additionally, van Pelt and others (2014) calculated that small-scale variability of snow accumulation had a negligible effect on the mean net mass balance in the accumulation zone and a negative impact of $-0.09\ \mathrm{m\,w.e.\ a^{-1}}$ in the ablation area.

Dadić and others (2010) is the only study thus far that has examined snow distribution on glaciers using a dynamic model. This study specifically looked at the effect of wind on snow accumulation and found that glacierized areas with the largest accumulation also experienced the lowest horizontal wind speeds and highest downward wind velocity. Preferential deposition was highest (positive or negative) in troughs located close to steep slopes, where updrafts and down drafts led to decreased and enhanced deposition, respectively. In general, the wind speed was controlled by small-scale topography and had a significant impact on accumulation.

Although there are still relatively few studies of snow distribution on glaciers, the work described above provides a good starting point for such investigations. Comparisons of variability between neighbouring glaciers and within a basin are both important areas of research.

1.5 Glaciers in the St. Elias Mountains

Snow data are generally sparse in mountain regions, especially those that are far from population centres (Marcus and Ragle, 1970). The St. Elias Mountains (Figure 1.6) are one such area. These mountains contain the largest non-polar ice field and the longest valley glaciers outside of Greenland and Antarctica (Marcus and Ragle, 1970; Danby and others, 2003). Steep climatic gradients across the mountains create sharp changes in glacier cover and mass balance (Clarke and Holdsworth, 2002). This region currently has the most negative mass budget and is the largest contributor to sea-level rise in the world (Kaser and

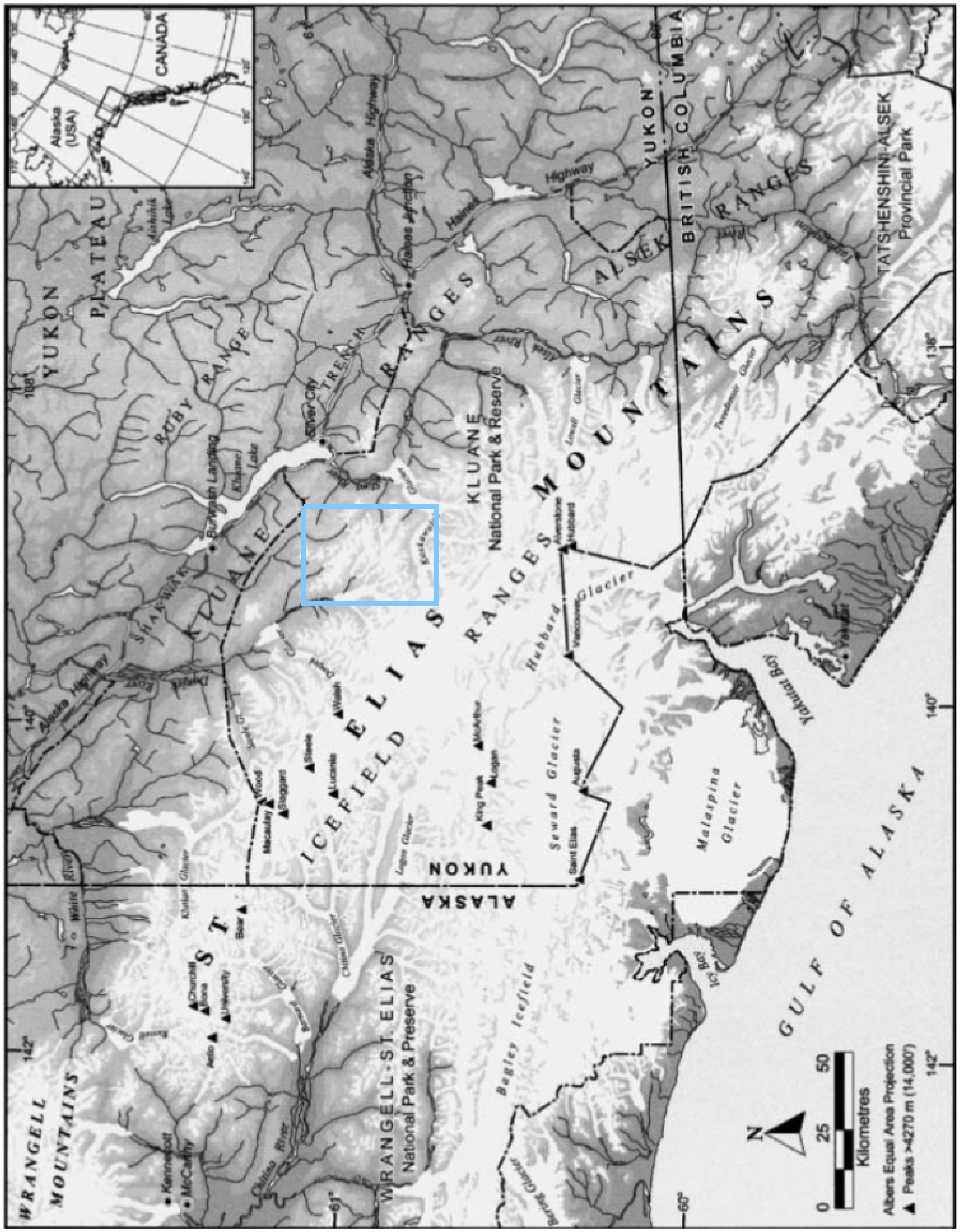

YUKON PLATEAU
RUBY RANGE
SHAKWAK TRENCH
KLUANE RANGES
ST. ELIAS MOUNTAINS
ICEFIELD RANGES
KLUANE National Park & Reserve
WRANGELL-ST. ELIAS National Park & Preserve
WRANGELL MOUNTAINS
ALSEK RANGES
TATSHENSHINI-ALSEK Provincial Park
YUKON
BRITISH COLUMBIA
ALASKA
GULF OF ALASKA
Kluane Lake
Aishihik Lake
Burwash Landing
Silver City
Haines Junction
Alaska Highway
Haines Highway
Malaspina Glacier
Seward Glacier
Hubbard Glacier
Bagley Icefield
Yakutat Bay
Yakutat
Icy Bay
Kennecott
McCarthy
Chitina River
White River
Logan
King Peak
McArthur
Augusta
Saint Elias
Hubbard
Alverstone
Vancouver
Lucania
Steele
Walsh
Wood
Slaggard
Macaulay
Bear
Churchill
Bona
University
Alaska (USA)
CANADA
N
0
25
50
Kilometres
Albers Equal Area Projection
▲ Peaks >4270 m (14,000')

Figure 1.6: Map of the St. Elias Mountains and surrounding area. Figure taken from Danby and others (2003).

others, 2006; Gardner and others, 2013). Understanding how local glacier mass balance is affected by distribution of snow is therefore critical for accurate predictions of glacier response to a warming climate.

The weather in the St. Elias varies considerably over the range. The west side of the mountains is characterized by a cool, Marine West Coast climate due to the influence of the Pacific Ocean, while the eastern side (just 250 from the coast) is considered subarctic (Marcus and Ragle, 1970). Taylor-Barge (1969) studied the relationship between synoptic weather conditions and basin weather conditions across the St. Elias Mountains. It was observed that the mountains are oriented perpendicular to frequent and intense storms that originate in the ocean, which results in considerable interaction between weather and topography. When weather moves from the Gulf of Alaska, it is orographically lifted, which creates significant precipitation. If the front is perpendicular to the mountains, it can be deflected north or south, depending on the upper atmospheric flow. Fronts that are more or less aligned parallel to the mountains or very strong perpendicular fronts travel without deflection. The fronts can also stall on the west side of the mountains. Occasionally, the fronts spill over the mountain divide (located to the west of the Kaskawulsh Glacier) and descend along the eastern side, which often results in decreased precipitation. The rain shadow is likely a major cause of differences in accumulation and equilibrium line altitude (ELA) between the two sides of the mountains~~—~~the marine side has an ELA of ~1100 m and the continental side has an ELA of ~2100 m, while at the same elevation there is three times more accumulation on the marine side (Marcus and Ragle, 1970).

Although the characterization of synoptic conditions by Taylor-Barge (1969) is useful, was conducted during the summer when weather conditions are considerably different than during winter. Taylor-Barge (1969) does note ~~though~~ that the weather patterns observed would likely be strengthened during winter because many of the spatial gradients are enhanced. The synoptic air masses present during the winter produce a strong temperature and moisture gradient, with warm, moisture-laden air coming from the Pacific Ocean and cold, dry air coming from the Mackenzie Basin. These gradients would likely result in even more precipitation and stronger winds. The presence of a high pressure Arctic system could decrease the ability of low-pressure systems to pass over the divide, leading to a further enhancement of precipitation on the western side of the mountains.

The study done by Taylor-Barge (1969) also identified weather patterns at multiple scales. Synoptic conditions, including front movement, affected regional-scale differences in weather and precipitation patterns. Watershed-scale topography was responsible for differences in weather between nearby basins and affected wind speed and direction most significantly. Point-scale topography had strong effects on snow accumulation. Orographic effects were found to be significant on all scales.

Research on snow distribution and glacier mass balance in the St. Elias is limited. The first significant investigations took place under Project Snow Cornice (Wood, 1948).

Researchers looked at snow accumulation and ice formation as well as ice-mass thermal regime, density and depth. Studies were conducted primarily on large glaciers such as the Kaskawulsh and Seward Glaciers and thus provided insights into large-scale accumulation patterns. This initiative was then followed by the Icefield Ranges Research Project (IRRP), which was established in 1961 (Danby and others, 2003). A number of subsequent long-term studies have been established in the St. Elias since IRRP (e.g. Clarke and others, 1984; Paoli and Flowers, 2009). For example, Wheler and others (2014) determined the end-of-winter accumulation for the mass balance of a small alpine glacier in the Donjek Range. The study measured snow depth at a number of fixed stakes and used a multiple linear regression model — that accounted for slope, curvature and elevation — to extrapolate these points and estimate basin-wide winter balance. Arendt and others (2008) also briefly studied the mass balance of a number of glaciers in the St. Elias.

Two ice cores have been retrieved from the St. Elias Mountains. The first one was taken from the summit of Mt. Logan (5340 m) in 1980 and was 103 m long. The accumulation history in this core has been used to study the local (Holdsworth and others, 1991) and regional (Moore and others, 2002) climate history. A second core, called the Eclipse core, was taken from a site 45 km northeast of Mt. Logan, 2 km lower in altitude, with an accumulation almost five times as large (Wake and others, 2002). This core is 160 m and has also been used for studying local and regional climate history (Wake and others, 2002).

A study done by Pomeroy and others (1999) looked at snow mass balance in a non-glacierized alpine basin within the St. Elias. It was found that wind had a significant impact on the distribution of snow — up to 79% of the snow was redistributed from alpine areas to (primarily) hillsides, where accumulation was tripled. In the study basin, measured accumulation ranged from 54% to 419% of the actual snowfall. However, in a subsequent study year, which had two large wet snow events, the redistribution of snow was minimal and accumulation variability was much lower. The type of snow and how susceptible it is to wind effects therefore also plays a critical role in distribution. Additionally, areas within the basin can have different accumulation patterns throughout the winter. One area within the basin studied by Pomeroy and others (1999) had almost no redistribution (despite heavy winds) from the beginning of winter through to March. After this, all of the snow was lost even though additional accumulation events occurred in the basin. This could indicate a dependence of redistribution on weather conditions such as temperature, or that a critical depth was reached that allowed for redistribution to occur. Sublimation was also observed to occur throughout the study period and since sublimation is several orders of magnitude faster when blowing snow is present (~20% of winter days in this study), it could have a significant impact.

~~There is clearly a strong need for a more comprehensive understanding of snow accumulation in the St. Elias Mountains~~. Although ~~a few~~ studies have examined accumulation, no studies have examined the distribution of snow and how it varies spatially. This is especially true of small alpine glaciers in the St. Elias Mountains, since most of the accumulation differences have been observed on large glaciers. It is likely that orographic lifting as well as wind redistribution and preferential deposition play major roles in determining accumulation on small alpine glaciers, so future studies should focus on the impact of these factors.

Table 1.2: Physical characteristics of the study glaciers and May 2016 winter-balance survey details, including number of snow-depth measurement locations along transects (n_{T}), total length of transects (d_{T}), number of combined snow pit and Federal Sampler density measurement locations (n_ρ) and number of zigzag surveys (n_{zz}).

	Location	**Elevation (m a.s.l)**			**Slope (°)**	**Area**	**Survey**	**Survey Details**			
	UTM Zone 7	*Mean*	*Range*	*ELA*	*Mean*	**(km^2)**	**Dates**	n_{T}	d_{T} (km)	n_ρ	n_{zz}
Glacier 4	595470 E 6740730 N	2344	1958–2809	~2500	12.8	3.8	4–7 May 2016	649	13.1	10	3
Glacier 2	601160 E 6753785 N	2495	1899–3103	~2500	13.0	7.0	8–11 May 2016	762	13.6	11	3
Glacier 13	604602 E 6763400 N	2428	1923–3067	~2380	13.4	12.6	12–15 May 2016	941	18.1	20	4

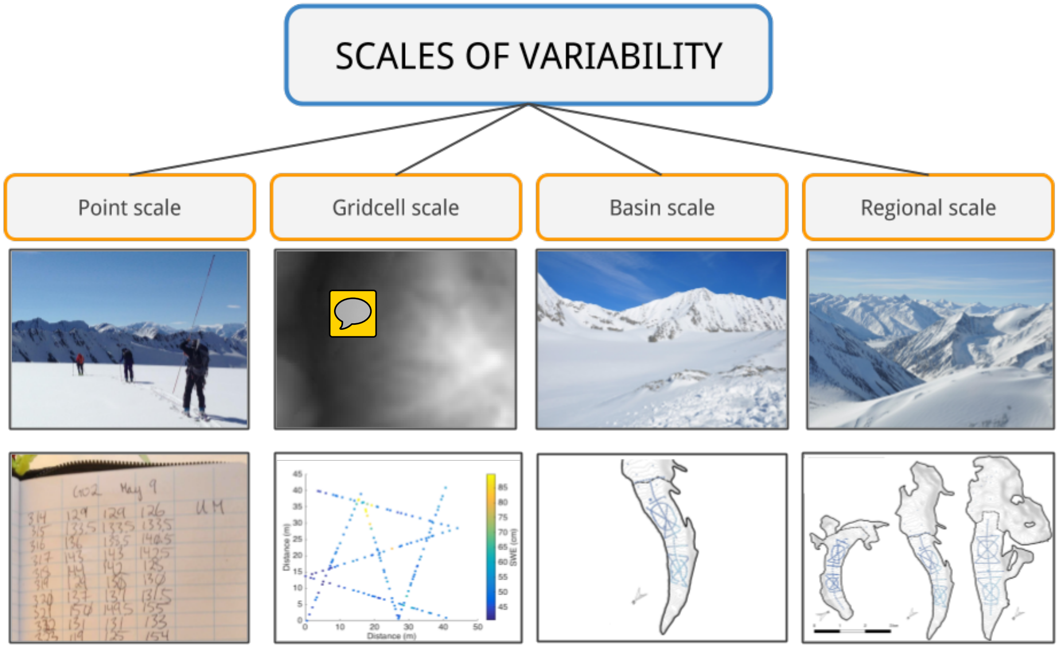

Figure 1.7: Visualization of four spatial scales investigated ~~in project~~. The lower panels show examples of the ~~amount of~~ data analysed at each scale.

1.6 Research scope

1.6.1 Overview of research

~~Our work~~ addresses the need for a multi-scale investigation of snow accumulation on alpine glaciers in the St. Elias Mountains. I focus on estimating winter surface mass balance (‘winter balance’), which is the net accumulation and ablation of snow over the winter season (Cogley and others, 2011), at multiple scales on three alpine glaciers in the Donjek Range (Table 1.2). The goals of this study are to (1) critically examine methods of converting direct snow depth and density measurements to distributed estimates of winter balance and (2) identify sources of uncertainty, evaluate their magnitude and assess their combined contribution to uncertainty in glacier-wide winter balance.

I focus on commonly applied, low-complexity methods of measuring and estimating winter balance in the interest of making my results broadly applicable. I conduct an extensive snow survey, using a combination of snow-depth probing and two snow density measurement techniques, on three alpine glaciers in the Donjek Range. A combination of statistical techniques, including basic statistics and regressions, is then used to investigate spatial variability at multiple scales. Throughout this thesis, four spatial scales that are relevant to estimating winter balance are discusses: point, gridcell, basin (or glacier-wide) and regional ~~scale~~ (Figure 1.7).

The thesis work is centred around the process of converting point-scale, direct measurements to estimates of glacier-wide winter balance using statistical models. The project is structured in four main stages (Figure 1.8). First, observations are described using basic statistics and a variety of density assignment methods are investigated. Second, regression and kriging methods are used to interpolate winter balance data. An evaluation of the various interpolation techniques is then done and significant topographic parameters are identified. Third, a Monte Carlo approach is used to investigate the effects of variability and uncertainty associated with the conversion of gridcell-scale winter balance values to an estimate of glacier-wide winter balance. Fourth, the transferability of statistical relationships between glaciers is examined and an winter-balance gradient on the continental side of the St. Elias Mountains is identified.

1.6.2 Thesis structure

The thesis is structured to follow the visual representation of the research ~~scope~~ presented in Figure 1.8. Chapter 2 provides a detailed description of the intended and executed experimental design as well as a description of how the observations are processed to produce data that can be analysed. Chapter 3 focuses on presenting snow depth and density ~~observations~~ as well as subsequent data processing. This chapter details various methods of assigning density values, converting snow depth and density to winter balance, as well as calculating topographic parameters used for interpolation. Chapter 4 details three interpolation methods used to obtain ~~a~~ distributed estimate of winter balance. Linear regression, simple kriging and regression kriging are compared and insights gained through the interpolation processes about controls on winter balance are discussed. Chapter 5 examines estimates of winter balance and how grid-scale variability, density assignment and data interpolation interact to create uncertainty in estimates of winter balance. Chapter 6 examines winter balance at the regional-scale. The transferability of linear regression models between glaciers is investigated and glacier-wide winter balances are related to the regional winter-balance gradient along the continental side of the St. Elias Mountains.

1.7 Summary

Snow accumulation plays a central role in alpine hydrology and has a prominent impact on glacier mass balance. In mountainous regions, accumulation is highly variable on point, hillslope, watershed and regional scales. The contribution of accumulation to glacier mass balance is controlled mainly by the distribution of snow. Processes such as orographic lifting, preferential deposition and wind redistribution, all arising from the interaction of atmospheric conditions and topography, strongly affect snow distribution. Statistical models have been used to relate meteorological and topographic variables to snow accumulation in order to better understand the effects of these processes. These models rely on accu-

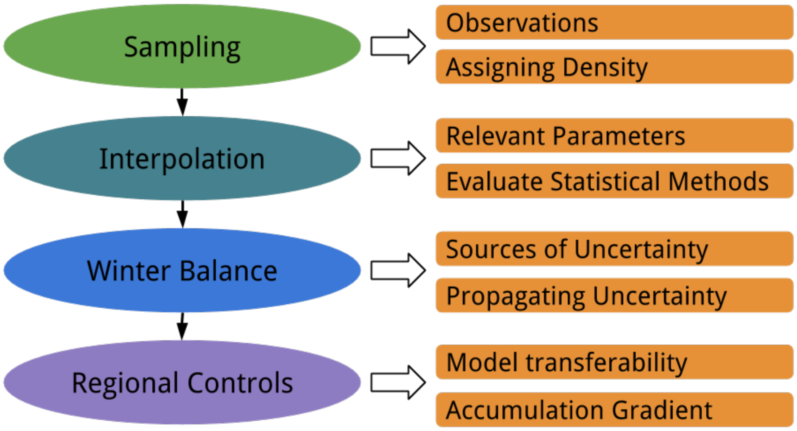
Sampling
Observations
Assigning Density
Interpolation
Relevant Parameters
Evaluate Statistical Methods
Winter Balance
Sources of Uncertainty
Propagating Uncertainty
Regional Controls
Model transferability
Accumulation Gradient

Figure 1.8: Visual representation of research project. General scope is described on the left (ovals) and specific investigations are shown on the right (squares).

rate measurement of snow distribution, which can be achieved by determining snow water equivalent values from snow density and depth. Results from previous studies of accumulation on glaciers have shown considerable spatial variability at many scales resulting from interactions between topography and atmospheric conditions.

Accumulation in the St. Elias Mountains is poorly understood. There is a need to quantify winter balance in this region and how it varies both between glaciers and within glacierized basins. My study is the first within the St. Elias Mountains to examine winter balance variability at the point, gridcell, basin and regional scales. Well-established methods are applied to estimate winter balance at multiple scales. The data are used to investigate the role of topography in determining snow distribution, uncertainty in estimating glacier-wide winter balance, the transferability of statistical relationship and regional differences in distributed winter balance. My comprehensive approach to examining spatial patterns in snow distribution on glaciers contributes to the current understanding of processes and parameters that affect winter balance variability on glaciers.